ORIGINAL PAPER

Modelling 3D metal cutting problems with the particle finite element method

J. M. Carbonell[1,2] · J. M. Rodríguez[4] · E. Oñate[2,3]

Abstract

This work presents the development of the Particle Finite Element Method (PFEM) for the modelling of 3D solid mechanics problems under cutting conditions. The study and analysis of numerical models reproducing the cut of a material is a matter of interest in several areas; namely, the improvement of the material properties, the optimization of the process and tool geometries and the prediction of unexpected failures. The analysis of bi-dimensional (2D) models is the most common approach for different reasons. Just focusing on the simulation point of view, it is the simplest procedure, the cheapest in terms of computational cost and sometimes the only feasible numerical solution. However, many industrial machining processes, such as cutting, blanking, milling and drilling have not a possible simplification to 2D models. Actually even a simple turning processes for non-orthogonal cuts can not be simplified to 2D. This work present an upgrade of the PFEM techniques in order to deal with the 3D machining problems. We present recent improvements in the finite element formulation, the meshing re-connections and the contact detection. By applying these developments the PFEM has the capability for modelling a wide range of practical machining processes. In this paper the capacity of the formulation and the accuracy of the results are analyzed and validated with some representative examples.

Keywords Machining · Three-dimensional modelling · Contact mechanics · Particle finite element method · PFEM

1 Introduction

Metal cutting is one of the most important operations for the manufacturing of components in various industries. For mechanical engineers it represents a challenging problem. It has fascinated researchers and practitioners for decades who have been investigating for the best possible characterization of the problem.

Several modelling techniques have been developed for the simulation of metal cutting problems during last years. Sum-marizing, they can be classified into methods supported by a mesh, and methods based in particles or mesh-free methods. The first group includes the Finite Element Method (FEM) in a Lagrangian, Eulerian and Arbitrary Lagrangian Eulerian formulations (ALE), the Multi-material Eulerian Method (MMEM), the Volume of Solid (VOS), the Material Point Method (MPM)and the Point in Cell (PiC). The second group of the particle-based methods includes: the Smoothed Particle Hydrodynamics (SPH), the Finite Point Method (FPM), the Constrained Natural Element Method (CNEM), the Discrete Element Method (DEM), the Maximum Entropy MeshFree method, and the Particle Finite Element Method (PFEM). Similar techniques with other names can be found in the literature. They represent the most important numerical approaches to the modelling of metal cutting problems. An extended review of the mentioned techniques can be found in [28]. The common denominator for most of the modelling techniques is the FEM, like it happens in the PFEM, which is the numericall technique object of study in the present work.

The Particle Finite Element Method (PFEM, www.cimne.com/pfem) has been widely studied in recent years. The general conclusion is that it is a good numerical method for

✉ J. M. Carbonell
cpuigbo@cimne.upc.edu

1   Faculty of Science and Technology, Department of Engineering, Universitat de Vic-Universitat Central de Catalunya (UVic-UCC), Vic, Spain

2   International Center for Numerical Methods in Engineering (CIMNE), Campus Nord UPC, Gran Capitán, s/n., 08034 Barcelona, Spain

3   School of Civil Engineering, Universitat Politècnica de Catalunya (UPC), Barcelona, Spain

4   School of Engineering, Department of Mechanical Engineering, Universidad EAFIT, Medellin, Colombia

the treatment of large deformation problems in continuum mechanics. There are many of examples of application of the PFEM in the field of fluid dynamics [15–17] and some in solid mechanics [14,21–27]. Several of the cited works present examples in 2D and some of them include particular 3D applications also. In most papers, nevertheless, it is taken for granted the easy extrapolation of the PFEM formulation for 3D problems without much details. Although there exist papers describing some details on the 3D aspects of the PFEM, as in [6,16,17], most of them are in the field of fluid-structure interaction. Some important particularities appear when treating 3D cases and they must be resolved for a proper functioning of the PFEM. In this work, the PFEM is applied to the simulation of 3D machining problems involving large deformations, contact conditions and thermal coupling situations.

1.1 Motivation

The motivation of this research comes from previous works of the authors in the field of forming and metal cutting problems (see for example [19,26]). Most of the cutting techniques employed in industry (i.e. milling and drilling in machining processes) have not a possible simplification to 2D. Advanced 3D modeling capabilities are needed for the numerical simulation of these problems. In this work we show that the PFEM is an excellent candidate for analysis of this class of complex metal forming processes.

Some of the numerical challenges related to the extension of the PFEM for 3D machining problems are related to geometrical aspects and other to numerical ones. The usual difficulties are the existence of a constrained Delaunay tessellation for 3D geometries, the poor accuracy of linear 4-noded tetrahedra elements, the computational cost of the numerical solution and the uncertain possibility of parallelize some of their parts. In this paper we address the solution to several of these challenges.

1.2 Objectives

This work aims to show that the PFEM is a good numerical technique that can be applied to a wide range of 3D machining problems, as well as to many other complex problems in solid mechanics. In the paper we detail the mathematical formulation of the PFEM for non linear solid mechanics problems, the treatment of thermo-mechanical coupling , necessary for the material behaviour characterization, and the formulation used in contact situations in order to reproduce the tool-workpiece interaction. The remeshing techniques have been redesigned and extended with the use of adaptive mesh refinement processes in order to improve robustness in 3D simulations. The purpose is to show that the PFEM can be applied satisfactorily to the 3D modelling and simulation of

practical machining problems. In the present work we are not dealing with the contact interactions that take into account friction, tool deformation and heat interchange in the contact area.

The paper is organized in three main sections. Section 2, introduces the basis of the PFEM and the PFEM solution flowchart. The PFEM formulations for thermal-mechanical coupled problems are explained in Sect. 2.2. The development of mixed formulation for linear simplex elements is presented in Sect. 2.3. The general settings for the modelling of a thermo-elasto-plastic material are introduced in Sect. 2.4, and the 3D mesh regeneration processes is explained in Sect. 2.5. In Sect. 3, the numerical techniques used for the contact detection and to impose the contact constraint are presented. Here the cutting tools are treated as rigid boundaries. In the last part of the paper (Sect. 4), validation examples are presented. The examples check the numerical behaviour of the 3D formulation, compare the solution of a cutting problem using 2D and 3D approaches, and show the capabilities of the PFEM for the 3D analysis of a machining problem with a complex material behaviour.

2 Three-dimensional PFEM

The PFEM has been broadly used in the field of fluid mechanics. Examples of 3D modeling of fluid dynamics with the PFEM can be found in [11,15,18]. The relevant aspects that can be mentioned when comparing 2D and 3D PFEM formulations are not very encouraging for the 3D case. Although 3D simulations are more impressive, the accuracy of the results is typically worse. This usually happens because 3D simulations are carried out using a smaller number of elements and a non-optimal distribution of them in the zones of interest which leads to a lower accuracy. The computational cost of a 3D computation is huge and the complexity of all related processes increase substantially. All operations related with geometry manipulations are crucial in the PFEM due to the remeshing steps involved in the technique. Some examples of 3D modeling of excavation problems using the solid mechanics version of the PFEM can be found in [6–8]. No other relevant applications are known for solving 3D problems in solid mechanics using the PFEM. In this type of problems, frictional contact situations are present which is an added complexity for the numerical simulation.

The modelling of cutting problems needs for a set of specific ingredients. Usually, materials are treated like continuum media, therefore the characterization of the behaviour is needed. The use of standard finite elements for the resolution of large deformation problems is a major advantage. However, the desirable description of the material domain must be calculated on a good shaped discretization. In the PFEM, the re-shaping of the computational domain is fun-
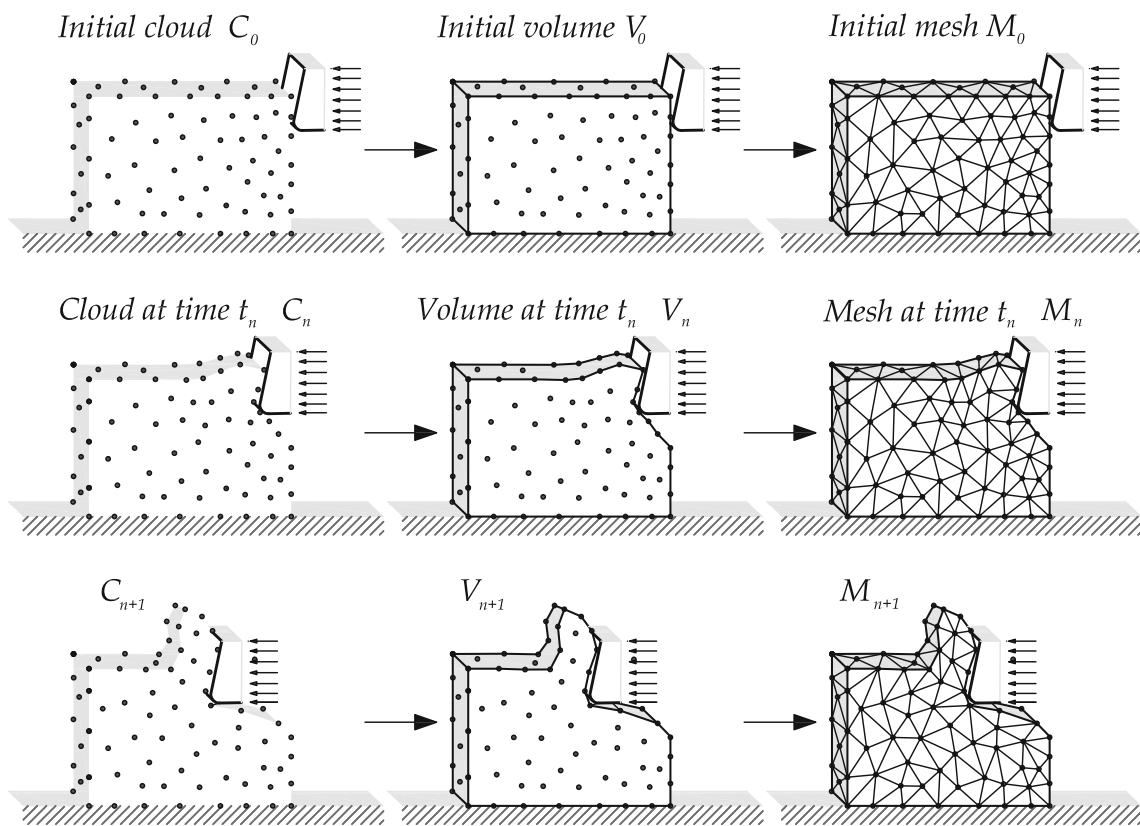
Fig. 1 Sequence of steps to update in time a "cloud" of nodes representing a workpiece in a progressively machining operation using the PFEM

damentally done via Delaunay tessellations from a cloud of particles, as described in Sect. 2.5. The original idea of the PFEM was to improve the mesh quality by performing a local re-tessellation of the domain only when is needed. This allows to capture large changes in the continuum domain and avoid global remeshing and interpolation from mesh to mesh.

2.1 PFEM solution flowchart

The PFEM uses a *updated Lagrangian* formulation for describing of the particle motion. From a *current configuration* of particles at time t a *new* or *updated configuration* is calculated at time $t + \Delta t$ (Fig. 1). In each new configuration a mesh discretizing the domain is generated for solving the governing equations in the standard FEM fashion. Therefore the FEM is used to solve the continuum equations that will be presented in Sect. 2.2. The nodes discretizing the analysis domain are treated as *material particles* which motion is tracked during the transient solution. The quality of the numerical solution depends on the discretization chosen as in the standard FEM. Adaptive mesh refinement techniques are used to improve the solution as described in Sect. 2.5.

For clarity purposes we will define the collection or *cloud of nodes* (C) belonging to the analysis domain, the *volume* (V) defining the analysis domain and the *mesh* (M) discretizing

the domain. The solution of the PFEM developed in this work involves the following steps:

1. At each time step there is an initial cloud of points defining the updated configuration of the domains. For instance C_n denotes the cloud at time $t = t_n$ (see Fig. 1).
2. The boundaries of the domains are identified as V_n. In this work, this step requires a refinement of the boundary faces from the previous configuration. Some boundaries may be severely distorted during the solution, including separation and re-entering of nodes. In these cases the α-*shape* method [42] is used for the boundary definition.
3. Discretize the continuum domains with a finite element mesh M_n. Perform a *constrained Delaunay* tessellation (Sect. 2.5).
4. Solve the Lagrangian equations of motion in the new mesh. Compute the state variables at the next *updated* configuration for $t + \Delta t$: displacements, pressure, temperature, stresses and strains, etc.
5. Move the mesh nodes to a new position C_{n+1} where $n+1$ denotes the time $t_n + \Delta t$. The updated positions are consequence of the solution process calculated in the previous step.
6. Go back to the first step and repeat the solution process for the next time step to obtain C_{n+2}.

Figure 1 shows a conceptual example of application of the PFEM to model the progressive cut of a solid mass (workpiece) under the action of an external object (cutting tool).

In the next sections we describe the solid mechanics formulation, the finite element discretization and the material models used.

2.2 Multiple field formulations

The problems under analysis here are characterized by the coupling of the mechanical and thermal part. Consequently, the equations describing the initial boundary value problem, are the ones which characterize large deformations of a material in a coupled thermo-mechanical situation. In solid mechanics, the balance equations are: the momentum, the mass conservation and the energy equations.

In order to improve the finite element accuracy in the modelling of complex material behaviours, mixed field formulations are considered. To keep the simplicity only two-field mixed formulations are used in this work. The most common one is the two-field displacement-pressure ($\mathbf{u}$-p) finite element formulation. The quasi-static mixed $\mathbf{u}$-p linear momentum equation in an updated Lagrangian scheme (i.e. expressing all quantities and their derivatives int the deformed configuration) may be written in its weak form as

$$\int_{V_t} \nabla \eta_{ij}\, s_{ij}\, dV_t + \int_{V_t} \nabla \eta_{ij}\, p\, \delta_{ij}\, dV_t - \int_{V_t} \eta_i b_i\, dV_t - \int_{\Gamma_N} \eta_i t_i^p d\Gamma = 0$$

(1)

$$\int_{V_t} q\, (p - \frac{1}{3}\, \sigma_{ii})\, dV_t = 0$$

(2)

An analogous mixed two-field form having the displacement $\mathbf{u}$ and the volumetric deformation ϕ as independent variables (the $\mathbf{u}$-ϕ formulation) can be expressed as

$$\int_{V_t} \nabla \eta_{ij}\, \check{\sigma}_{ij}\, dV_t - \int_{V_t} \eta_i b_i\, dV_t - \int_{\Gamma_N} \eta_i t_i^p d\Gamma = 0$$

(3)

$$\int_{V_t} q\, (J - \phi)\, dV_t = 0$$

(4)

where $\mathbf{u}(\mathbf{x}, t)$ the displacement field in the current configuration $\mathbf{x}$ at time t and $p(\mathbf{x}, t)$ the pressure. V_t is the volume occupied by the solid in the current configuration, σ_{ij} is the Cauchy stress tensor and s_{ij} is its deviatoric part. b_i are the external body forces and t_i^p the prescribed surface forces, $\nabla \eta_{ij}$ is a virtual strain field and η_i are the space weighting functions for the displacement field.

For the $\mathbf{u}$-ϕ formulation, $J = det(\mathbf{F})$ is the determinant of the deformation gradient, ϕ is the volumetric deformation and $\check{\sigma} = \sigma(\check{\mathbf{F}})$ is the Cauchy stress evaluated via the deformation gradient $\check{\mathbf{F}}$. q are the space weighting functions for

the pressure or for the volumetric deformation respectively. The deformation gradient is defined as

$$\check{\mathbf{F}} = \mathbf{F}_v \mathbf{F}_d = \phi^{\frac{1}{3}} \mathbb{1}\, (det(\mathbf{F})^{-\frac{1}{3}} \mathbf{F}) = \left(\frac{\phi}{J}\right)^{\frac{1}{3}} \mathbf{F}$$

(5)

being $\mathbf{F}_d = J^{-\frac{1}{3}} \mathbf{F}$ the volumetric deviatoric part of the deformation gradient and the volumetric part $\mathbf{F}_v = \phi^{\frac{1}{3}} \mathbb{1}$ is replaced by the independent volumetric deformation.

The mass conservation equation is expressed by $\rho_0 = J\rho$. The energy equation may be written in weak form as

$$\int_{V_t} \hat{w} \rho\, c\, \frac{d\theta}{dt}\, dV_t + \int_{V_t} \frac{\partial \hat{w}}{\partial x_i} (k\, \frac{\partial \theta}{\partial x_i})\, dV_t - \int_{V_t} \hat{w}\, \mathcal{D}_{int}\, dV_t$$
$$+ \int_{\Gamma_{N_\theta}} \hat{w}\, q_n\, d\Gamma = 0$$

(6)

where $\theta(\mathbf{x}, t)$ is the temperature field, ρ is the density, c the specific heat, and k the thermal conductivity. $\mathcal{D}_{int}$ is the term that accounts for the mechanical dissipation, the structural elastic heating and the possible thermal source and q_n is the flux in the boundary. Finally, $\hat{w}$ are the space weighting functions for the temperature.

The initial conditions are prescribed by assigning the initial displacement $\mathbf{u}_0(\mathbf{x})$, the initial velocity $\mathbf{v}_0(\mathbf{x})$ and the initial temperature $`_0(\mathbf{x})$ at the Dirichlet and Neumann boundaries Γ_D and Γ_N for the mechanical part, respectively, as appropriate, i.e.

$$\mathbf{u}(\mathbf{x}, t) = \bar{\mathbf{u}}(\mathbf{x}, t)\ \forall \mathbf{x} \in \Gamma_D$$
$$\mathbf{v}(\mathbf{x}, t) = \bar{\mathbf{v}}(\mathbf{x}, t)\ \forall \mathbf{x} \in \Gamma_D$$
$$\sigma(\mathbf{x}, t) \cdot \mathbf{n} = \bar{\mathbf{h}}(\mathbf{x}, t)\ \forall \mathbf{x} \in \Gamma_N$$

(7)

here $\bar{\mathbf{u}}(\mathbf{x}, t)$, $\bar{\mathbf{v}}(\mathbf{x}, t)$ and $\bar{\mathbf{h}}(\mathbf{x}, t)$ are prescribed fields, $\mathbf{n}$ denotes the out-ward normal to the boundary and $\Gamma_D \cup \Gamma_N = \partial \Omega$. The boundary conditions for the thermal part are imposed as

$$\theta(\mathbf{x}, t) = \bar{\theta}(\mathbf{x}, t)\ \forall \mathbf{x} \in \Gamma_{D\theta}$$
$$-k\nabla \theta \cdot \mathbf{n} = \bar{\mathbf{q}}(\mathbf{x}, t)\ \forall \mathbf{x} \in \Gamma_{N\theta}$$

(8)

where $\bar{\theta}(\mathbf{x}, t)$ and $\bar{\mathbf{q}}(\mathbf{x}, t)$ are prescribed fields assigning temperature and flux, $\mathbf{n}$ denotes the out-ward normal to the boundary and $\Gamma_{D\theta}$ and $\Gamma_{N\theta}$ with $\Gamma_{D\theta} \cup \Gamma_{N\theta} = \partial \Omega$ represent the Dirichlet and Neumman boundaries for the thermal part.

2.3 3-Simplex elements

One of the fundamentals of the PFEM is the use of simplices for the discretization of the weak form of the governing equations. For 3D problems the 3-simplex element is a tetrahedron. The use of simplices in the PFEM implies using

linear interpolations for approximating the fields describing the primary variables u - p - θ or u - ϕ - θ for the formulations presented in Sect. 2.2. From the point of view of efficiency, using 3-simplices with linear interpolation has some advantages: linear tetrahedra are computationally cheaper and geometrically simpler. However, it can turn to a penalization when the modelling demands for high accuracy.

In order to improve the well known weaknesses of linear tetrahedra, we have focused on formulations with multiple fields. These formulations solve some numerical deficiencies of the mentioned elements but need extra mathematical considerations in order to get coherent and stable solutions. In our approach, linear shape functions are used for all the primary variables of the mixed formulations and this creates a numerical inconsistency in the variational formulation [3] which has to be attended via stabilized techniques. The formulations presented in Sect. 2.2, are stabilized using is the polynomial pressure projection (PPP) approach introduced by *Bochev* [4], previously applied to stabilize Stokes Eqs. [4,10]. The PPP approach is probably the simpler way to find out a stable solution for a mixed equal-order interpolation of the scalar and vector fields. Its main ingredient is to use a L_2 projection of the scalar variables (volumetric deformation or pressure variables).

The method modifies the mixed variational equation (i.e. the pressure continuity equation) using local L_2 polynomial pressure projections of the pressure variable. The application of the projections in conjunction with the minimization of the problem field mismatch, eliminates the inconsistency of equal-order approximations and leads to a stabilized and consistent variational formulation.

One of the advantages of the PPP approach is that it does not require specification of a mesh-dependent stabilization parameter, or the calculation of higher order derivatives.

The PPP method uses a projection on a discontinuous space and can be implemented at element level. As a consequence, the implementation of this stabilization scheme reduces to a simple modification of the weak form of the continuity equation (the incompressibility constraint).

Given a function $\phi \in L_2$ (being ϕ the volumetric deformation), the L_2 projection operator $\breve{\phi} : L_2 \rightarrow Q^0$ is defined by

$$\int_{V_t} \breve{q}\,(\phi - \breve{\phi})dV_t = 0 \quad \forall \breve{q} \in Q^0 \tag{9}$$

where $\breve{\phi}$ is the best approximation of the scalar variable ϕ in the space of polynomials of order $\mathcal{O}(Q^0)$. V_t is the volume of the domain at the current configuration.

To stabilize the mixed form given by Eqs. (1) and (2) and Eqs. (3) (4), we add the following projection operator to Eq. (2) and (4):

$$\int_{V_t} (q - \breve{q})\frac{\alpha_s}{\mu}(\phi - \breve{\phi})dV_t = 0 \tag{10}$$

where α_s is the stabilization parameter (usually $\alpha_s = 1$) and μ is the shear modulus. Note that α_s does not depend on the mesh, it is only a parameter to increase of decrease the amount of diffusion added by the stabilisation procedure. The stabilisation therm can be formulated for the pressure field replacing the volumetric deformation ϕ by the pressure p. In Eq. (10), q are the space weighting functions for the pressure, or for the volumetric deformation, and $\breve{q}$ the projection of the weighting functions.

Adding the PPP stabilization to the **u**-p formulation into Eqs. (1) and (2), the weak form of the balance equations can be written as :

$$\mathbf{F}_{\mathbf{u},\text{int}}(\mathbf{u}, p) - \mathbf{F}_{\mathbf{u},ext} = 0 \tag{11}$$
$$\mathbf{F}_{p,pres}(p) - \mathbf{F}_{p,vol}(\mathbf{u}) + \mathbf{F}_{p,stab}(p) = 0 \tag{12}$$

where

$$\mathbf{F}_{\mathbf{u},int}(\mathbf{u}, p) = \int_{V_t} \mathbf{B}_u{}^T (\mathbf{s} + p)\, dV_t \tag{13}$$

$$\mathbf{F}_{\mathbf{u},ext} = \int_{V_t} \mathbf{N}^T \mathbf{b}\, dV_t - \int_{\Gamma_\sigma} \mathbf{N} t^p\, d\Gamma_\sigma \tag{14}$$

$$\mathbf{F}_{\mathbf{p},pres}(p) = \int_{V_t} \frac{1}{k}\mathbf{N}\mathbf{N}^T p\, dV_t \tag{15}$$

$$\mathbf{F}_{\mathbf{p},vol}(\mathbf{u}) = \int_{V_t} \mathbf{N}^T \left(\frac{1}{3}\mathbb{1} : \boldsymbol{\sigma}\right) dV_t \tag{16}$$

$$\mathbf{F}_{p,stab}(p) = \int_{V_t{}^{(e)}} \frac{\alpha_s}{\mu} \mathbf{p}^{(e)} \left(\mathbf{N}^{(e)}\mathbf{N}^{T\,(e)} - \tilde{\mathbf{N}}^{(e)}\tilde{\mathbf{N}}^{T\,(e)}\right) dV_t{}^{(e)} \tag{17}$$

where k is the material bulk modulus, $\mathbf{N}$ are the global shape functions and $\mathbf{B}_u$ is the strain-displacement matrix that contains the derivatives of the shape functions used in the interpolation of the problem variables. $\tilde{\mathbf{N}}^{(e)}$ contain the set of polynomials of order 0.

Analogously, the discrete form of the stabilized Eqs. (3) for the **u**-ϕ formulation, can be written as :

$$\mathbf{F}_{\mathbf{u},\text{int}}(\mathbf{u}, \phi) - \mathbf{F}_{\mathbf{u},ext} = 0 \tag{18}$$
$$\mathbf{F}_{J,J}(\phi) - \mathbf{F}_{J,\phi}(\mathbf{u}) + \mathbf{F}_{\phi,stab}(\phi) = 0 \tag{19}$$

where

$$\mathbf{F}_{\mathbf{u},int}(\mathbf{u}, \phi) = \int_{V_t} \mathbf{B}_u{}^T \breve{\boldsymbol{\sigma}}\, dV_t \tag{20}$$

$$\mathbf{F}_{J,J}(\phi) = \int_{V_t} \mathbf{N}\mathbf{N}^T \frac{\phi}{J}\, dV_t \tag{21}$$

$$\mathbf{F}_{J,\phi}(\mathbf{u}) = \int_{V_t} \mathbf{N}^T J\, dV_t \tag{22}$$

$$\mathbf{F}_{\phi, stab}(\phi) = \int_{V_t^{(e)}} \frac{\alpha_s}{\mu} \boldsymbol{\phi}^{(e)} \left(\mathbf{N}^{(e)} \mathbf{N}^{T\,(e)} - \tilde{\mathbf{N}}^{(e)} \tilde{\mathbf{N}}^{T\,(e)} \right) dV_t^{(e)} \tag{23}$$

Inserting the finite element interpolation into ((6)) yields

$$\mathbf{F}_{\theta, dyn}(\dot{\theta}) - \mathbf{F}_{\theta, int}(\theta) + \mathbf{F}_{\theta, ext} = 0 \tag{24}$$

where

$$\mathbf{F}_{\theta, int}(\theta) = \int_{V_t} k \mathbf{B}_\theta^T \mathbf{B}_\theta \, dV_t - \int_{V_t} \mathbf{N}^T Q \, dV_t \tag{25}$$

$$\mathbf{F}_{\theta, ext} = \int_{\Gamma_{\mathbf{q}}} \mathbf{N}^T (\mathbf{q}^p \cdot \mathbf{n}) \, d\Gamma_{\mathbf{q}} \tag{26}$$

$$\mathbf{F}_{\theta, dyn}(\dot{\theta}) = \int_{V_t} \rho c \, \mathbf{N} \mathbf{N}^T \dot{\theta} \, dV_t \tag{27}$$

where $\mathbf{B}_\theta$ is the global gradient-temperature that contains the derivatives of the shape functions used in the interpolation of the temperature field.

A Backward Euler method is used to discretize Eq. ((24)) in time, giving

$$\mathbf{F}_{\theta, dyn}(\dot{\theta}_{n+1}) - \mathbf{F}_{\theta, int}(\theta_{n+1}) + \mathbf{F}_{\theta, ext} = 0 \tag{28}$$

where

$$\dot{\theta}_{n+1} = \frac{\theta_{n+1} - \theta_n}{\Delta t} \tag{29}$$

and Δt is the size the length of the time interval

In finite element computations, the force vectors presented in Eqs. (11), (18) are obtained as the assemblies of element vectors. The isothermal split method is used to couple the mechanical and thermal parts of the problem [32]. In the PFEM, force vectors are evaluated in the support mesh of linear tetrahedra using standard Gaussian quadratures. For dynamic analyses implicit time integration of the kinematic variables are used via the standard *Newmark-β* method. In some problems a *line-search* strategy is utilized to ensure convergence of the solution.

2.4 Material models

The state of the art in material modelling of large deformation elasto-plasticity has two main frameworks [30–33]. One is based on an additive decomposition of the plastic and elastic strains; this is possible employing the use of hypo-elastic rate constitutive models. They are based in an extension of the small strain formulation adding some necessary terms in order to deal with rigid body rotations. These terms are also needed to ensure the objectivity of the resulting stress increment [1,33]. Usually this is a good approach for finite element methods using velocity formulations [1,33].

In the second approach, a multiplicative decomposition of the deformation gradient and a hyper-elastic response are assumed. This approach is best suited to problems involving both large displacements and large deformations [30–33] and is the one adopted for the PFEM when the displacement vector is one of the primary variables.

The total deformation gradient, $\mathbf{F}$, is decomposed multiplicatively into an elastic and plastic part: $\mathbf{F} = \mathbf{F}^e \mathbf{F}^p$. The elastic part applies to an intermediate configuration of irreversible (plastic) deformation. The elastic deformation gradient may itself be decomposed into a volumetric and deviatoric part: $\mathbf{F}^e = \mathbf{F}_v^e \mathbf{F}_d^e$. The volumetric part is given by $\mathbf{F}_v^e = (J^e)^{\frac{1}{3}} \mathbb{1}$ and the deviatoric part by $\mathbf{F}_d^e = \mathbf{F}^e (J^e)^{-\frac{1}{3}} \mathbb{1}$ where $J^e = det(\mathbf{F}^e)$ is the elastic Jacobian. Note that in the $\mathbf{u}\text{-}\phi$ formulation the decomposition of the elastic deformation gradient is $\breve{\mathbf{F}}^e = (\phi/J^e)^{\frac{1}{3}} \mathbf{F}^e$, shown in Eq. (5).

Elastic deformation is assumed to be hyper-elastic, with uncoupled volumetric and deviatoric responses. The hyper-elastic stress-strain realationship is expressed as

$$\boldsymbol{\tau} = 2 \rho_0 \, \mathbf{b}^e \, \partial_{\mathbf{b}^e} \psi(\mathbf{b}^e) = 2 \rho_0 \, \mathbf{b}^e \, \partial_{\mathbf{b}^e} (U(J^e) + W(\bar{\mathbf{b}}^e)) \tag{30}$$

where $\boldsymbol{\tau}$ if the Kirchhoff stress tensor, $\mathbf{b}^e = \mathbf{F}^e \mathbf{F}^{eT}$ and $\bar{\mathbf{b}}^e = \mathbf{F}_d^e \mathbf{F}_d^{eT}$ are the elastic left Cauchy Green tensor and its deviatoric part, respectively. The elastic part of the free energy $\psi(\mathbf{b}^e)$ is uncoupled into the volumetric and deviatoric response described by the functions $U(J^e)$ and $W(\bar{\mathbf{b}}^e)$, respectively.

When temperature effects must be considered, a function describing the thermo-mechanical coupling is needed. This is $M(\theta, J^e)$ which is added as a part of the free-energy function and provides the potencial for the associated elastic structural entropy. Thus the expression of the energy function $\psi(\mathbf{b}^e)$ is

$$\psi(\mathbf{b}^e) = U(J^e) + W(\bar{\mathbf{b}}^e) + M(\theta, J^e) \tag{31}$$

Extending the formulation to thermo-plasticity, the plastic response must be characterized by a function $K(\bar{e}^p, \theta)$, which is a nonlinear function of the equivalent plastic strain $\bar{e}^p$ and the temperature θ. This function describes the isotropic strain hardening via the relation $\beta = -\partial_{\bar{e}^p} K(\bar{e}^p, \theta)$. The potential for the purely thermal entropy must be also considered by adding a function $T(\theta)$. The complete form of the stored energy for the characterization of the stress response can be written as

$$\psi = U(J^e) + W(\bar{\mathbf{b}}^e) + M(\theta, J^e) + T(\theta) + K(\bar{e}^p, \theta) \tag{32}$$

In general the plastic part also requires the specification of a yield criterion, $\Phi(\tau, h)$, a hardening law, $h(\bar{e}^p, \theta)$ and a flow rule, g, in addition to the Kuhn-Tucker conditions [33]. Explicit forms of these functions can be found in [13,32].

In the examples presented in this work we have considered the classical *Mises-Hubber* yield function, expressed in terms of the Kirchhoff stress tensor, as:

$$\Phi(\tau, \bar{e}^p, \theta) = \|dev(\tau)\| - \sqrt{\frac{2}{3}} \left(\sigma_y + \beta\right) \le 0 \qquad (33)$$

where σ_y is the flow stress and $\beta = -K'(\bar{e}^p, \theta)$ is the isotropic nonlinear hardening modulus.

Numerous empirical and semi-empirical flow stress models have been proposed. The strain-rate dependent phenomenological model developed by *Johnson and Cook* [13] and the rate independent model developed by *Voce* [34] will be used in this work.

The *Johnson-Cook* model describes the flow stress of the material as the product of several terms involving a constant A, the initial yield strength of the material at room temperature and a reference strain rate, i.e.

$$\left(\sigma_y + \beta\right) = A\left(1 + \frac{B}{A}\varepsilon^n\right)\left(1 + C \ln \dot{\varepsilon}^*\right)\left(1 - \theta'^m\right) \quad (34)$$

where ε is the equivalent plastic strain, $\dot{\varepsilon}^* = \dot{\varepsilon}/\dot{\varepsilon}_0$ is the strain rate non-dimensionalized by the reference strain rate, and B, C, m and n are fitting constants.

Voce [34] proposed an exponential form for hardening. The strain hardening law interrelating true stress $\left(\sigma_y + \beta\right)$ and true plastic strain $\bar{\varepsilon}_p$ is expressed as

$$\left(\sigma_y + \beta\right) = (K_{\text{inf}} - (K_{\text{inf}} - \sigma_0)e^{-\delta\bar{\varepsilon}_p} + H\bar{\varepsilon}) * (1 - w_0(\theta - \theta_0)) \qquad (35)$$

where K_{inf} is the saturation stress, σ_0 is the true stress at the onset of plastic deformation and H is the linear hardening modulus. The constant δ determines the rate at which the stress σ_0 moves from its initial value tends to reach steady state or saturation stress K_{inf}. The material property w_0 describes the thermal softening of the material of interest and θ and θ_0 are the current and the reference temperature respectively. It is important to remark that if $n = 1$, $m = 1$ and $C = 0$, the *Johnson-Cook* material model recovers the *Voce* model.

Extended information of these isotropic hardening laws can be found in [23,26,32,36].

Alternatives to the use of phenomenological models for the treatment of plasticity has been investigated. In order to get a more realistic description of the deformation, the underlying the physics of the micro-structural evolution are introduced as a part of the constitutive model equations. These are called physically-based models. One of the advantages they exhibit is that they can be extrapolated outside the calibration range. In this work we have used the physically-based plasticity model based on dislocation density and vacancy concentration. This model was previously used in 2D metal cutting simulations in [24,35].

2.5 3D delaunay tessellation

In Sect. 2.3 we introduced the 3-simplex element that the PFEM typically uses for computing the continuum solution. One of the reasons for using this element type is the need for the continuous remeshing required by the method in order to adapt the domain geometry to the solution. In the PFEM the domain is seen as a set of lagrangian points, called particles. These particles store the information needed to determine the geometrical limits the domain, and the values of the material and kinematic variables (Fig. 1).

All the characteristics described by the particles are preserved after the tessellation of the domain every time a new mesh is sought. In our work we use a 3D Delaunay tessellation that will provide us with a thetraedral mesh discretizing the analysis domain [5,9,12,29]. The Delaunay tessellation has the properties of reconnecting a set of points maximizing the dihedral angles of the tetrahedral planes for the resultant mesh. Using this algorithm, a continuous re-connection of the particles configuring the domain is performed. In every remeshing step a finite element mesh with optimal shape is obtained for the discretization and resolution of the weak form of the governing equations.

One of the particular advantages of the PFEM is the concept of particle container. When the continuum domain is rebuilt, the information transfer is minimized because the particles are not modified. There is only transfer of information when the domain is refined and new particles are considered. This concept of particles container is modified when elemental information is needed for the solution of the material behaviour. Thus, in solid mechanics, the essence of the PFEM is modified versus fluid dynamics applications, where almost every model feature is intrinsically stored in the particles.

In the literature of the PFEM for solid mechanics, there are several approaches to manage the transfer of information between mesh elements and particles [6,8,23]. The goal is to minimize the loss of information due to continuous remeshing. Following this objective a particular transfer scheme for solid mechanics problems has been designed. The procedure is based in the following steps: (1) add particles where needed, (2) remove not needed or collapsing particles, (3) reconnect the cloud of particles, (4) improve collocation and set information to new elements. All steps are described in detail in Box 1. The previous mesh information is not dismissed until the process ends and all information is transferred from the mesh to the particles.

The mesh generation steps in Box 1 include new enhanced processes which improve the geometry of the boundary,

reduce the computational cost and increase the mesh quality. From these processes we can remark:

- **Boundary improvement**: When particles are inserted in a curved boundary, neighbour node distances and surface normals are used to perform Hermite interpolation and correct the particle insertion position.
- **Reducing number of mesh elements**: Particles are usually removed when they get too close to each other. In order to reduce the computational cost, particles can also be removed if the error in the solution is small. This is performed by computing error estimators in patches of elements surrounding a node. The error estimator is calculated for each element of the patch as $\epsilon_\sigma = \|\sigma - \sigma_h\|$ (see Zienkiewicz and Zhu [43,44]). The values chosen for the variable σ are the norm of the isochoric-stress or the equivalent plastic strain. When the mean value of this error, for all elements surrounding a particle, is smaller than a given tolerance ($\bar{\epsilon}_\sigma < \varepsilon_{\text{tol}} \approx 2\%$) the particle is removed.
- **Increase mesh elements quality**: Elements in plasticity regions suffer large distortions. The reconnection of particles using a *Delaunay* tesselation solve this effect partially. The quality of the elements in these areas is improved by performing a local *Laplacian smoothing* [20] of the updated particle positions after the tessellation. The *Laplacian smoothing* process is applied when particles are inserted to the model at the reconnection step and the mean value of the equivalent plastic strain is larger than a threshold value, a common value is $\bar{e}^p \geq 0.5$. This means that re-collocation of particles only applies to plasticity zones. When modelling metal cutting problems, these zones are the ones close to the tool tip.

We remark that in this work the transfer is made straight from the previous Gauss points to the Gauss points of the new elements. When the mesh does not change this transfer ensures that equilibrium is preserved after the tetrahedralization without adding diffusion to the results. When the mesh changes, the equilibrium is perturbed locally in areas where introduction and deletion of particles occur and the transformation of the information is unavoidable. FEM and PFEM solutions applying this transfer scheme were compared in previous works showing negligible effects in the final results [23,27].

One of the main advantages of the proposed strategy is that it is not necessary to create a complete new mesh at each time step. During the remeshing process the quality of the previous discretization can be improved with the addition and removal of particles using a local *Delaunay* tessellation.

PFEM: Computing Domain generation steps

Reference mesh elements $\mathcal{M}_{ref}^n$ and **nodes (cloud of particles)** $\mathcal{P}_{ref}^n$ at t^n.

1. Refine reference mesh → **using mesh elements** $\mathcal{M}_{ref}^n$.
   - Refine body elements. Insert new particles inside the domain.
   - Refine distorted boundary. Insert new particles and reconnect surface boundary faces (important for conforming boundaries).

   *$Criterion$: based on size, plastic dissipation or mean stress values

   *$Position$: new particles are inserted in the middle of the largest edge; particles at boundary must preserve surface curvature.
   (Note: other positions are the center of the largest triangular face or in the center of the tetrahedron).

2. Remove particles that are too close → **using particle distances** $\mathcal{P}_{ref}^n$.

   *$Optional$: remove particles using error estimators. Error estimators based on plastic strain values or on the norm of the isochoric stresses. A particle is removed if all previous finite elements joined to that particle have an error value less or equal to a given tolerance (see Zienkiewicz and Zhu [43,44]).

3. Nodal variables are interpolated to the new particles using elemental shape functions.

Updated cloud of particles $\mathcal{P}_{cur}^n$ and **boundary faces** $\mathcal{F}_{cur}^n$ at t^n.

- Perform a **constrained *Delaunay*** tetrahedralization using the updated boundary faces $\mathcal{F}_{cur}^n$ and the updated cloud of particles $\mathcal{P}_{cur}^n$.

  *$Note$: if the "constrained" *Delaunay* tetrahedralization is not possible, auxiliary boundary points are added $\mathcal{P}_{cur}^n \rightarrow \hat{\mathcal{P}}_{cur}^n$, boundary faces are regenerated $\mathcal{F}_{cur}^n \rightarrow \hat{\mathcal{B}}_{cur}^n$, and $\mathcal{F}_{cur}^n := \hat{\mathcal{F}}_{cur}^n$, $\mathcal{P}_{cur}^n := \hat{\mathcal{P}}_{cur}^n$.

Current mesh elements $\mathcal{M}_{cur}^n$ and **particles** $\mathcal{P}_{cur}^n$ at t^n

1. Estimate the mesh quality. If mesh quality is less or equal than a given tolerance, apply a local *Laplacian smoothing* [20] of the updated particle positions.
   (a) Find smoothed distribution of particles in the new mesh.
   (b) Transfer particle information (displacement, pressure/volumetric deformation, temperature) to the new particle positions by interpolation with the shape functions.
   (c) Calculate the global coordinates of the integration points in the new mesh.

2. Update the internal variables → **using the reference mesh** $\mathcal{M}_{ref}^n$.
   *$Criterion$: the local information of finite element in the new mesh is given by the closest finite element of the reference mesh.

   *$Note$: step 1 in the **current mesh** $\mathcal{M}_{cur}^n$ is optional.

Updated mesh elements $\mathcal{M}_{cur}^n$ → compute next step t^{n+1} → $\mathcal{M}_{ref}^{n+1} := \mathcal{M}_{cur}^{n+1}$.

Box 1: Flowchart of the domain regeneration process for the PFEM.

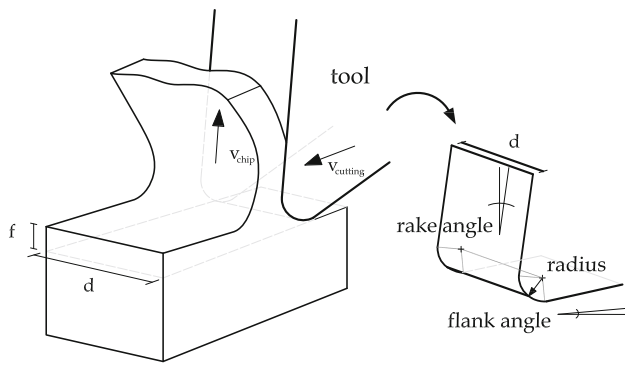**Fig. 2** Linear cutting test model

Fig. 3 Rigid tool definition

3 Treatment of the mechanical contact

Modelling of machining processes needs for the treatment of the interaction of a cutter and a solid piece. Seeking for simplicity, the cutter will be considered as a rigid boundary contacting the solid piece. The solid piece is the deformable body that will be modelled using the PFEM. Considering the cutter as a rigid body has certain advantages, the main one being that the geometry is fixed and can be characterized in an easier way. As a counterpart, when rigid tools are used heat generation by friction and the transfer of temperature between domains are usually not considered.

3.1 Models for rigid tools

Usually there are two ways to define a rigid cutter, the first one is using a finite element mesh to define the cutter boundary. When the tool surface is discretized with a standard triangular mesh there is no continuity from one element to another. This discrete interface gives a non-smooth contact force profile. The lack of continuity typically degrades the convergence of the solution. In order to avoid this problem, we have chosen another alternative. The rigid boundary is defined by the mathematical description of the surface. With this approximation the drawbacks coming from the treatment of contact between discrete face elements are overcome. This also allows to obtain a good definition of the contact forces and a good characterization of the contacting geometry. The mathematical description of the rigid boundary surface is given by a parametrization of the cutter surface.

This approach is valid for the linear cutting test models that we analyse in this work. The model is depicted in Fig. 2, it is ease to see that the tool can be considered as a rigid wall described by a two planes and a tip semi-circle.

3.2 Contact detection

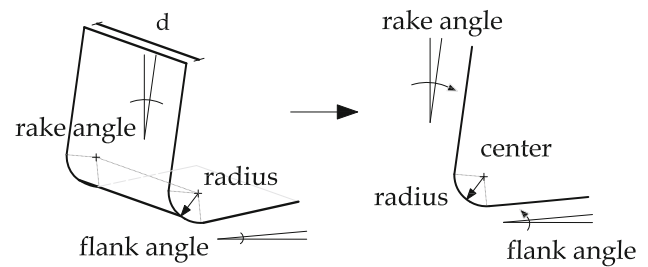The geometry descring a cutting tool can be characterized with three parameters: the tip radius, the angle of the rake face (rake angle) and the angle of the flank face (flank angle) (Fig. 3). These three parameters define a circle (or a cylinder in 3D) and two planes tangent to that circle and the geometry is mathematically determined. For the contact detection, one must identify what are the exterior and the interior parts of the tool. With these characteristics the contact detection is straightforward: when a particle belonging to the boundary of the workpiece is going to exceed the described rigid contour, that particle is assumed to be in contact with the tool.

A particle can enter to contact with the tip, the rake face or the flank face. Depending on the contact zone, the contact force direction changes. Therefore, it is important to detect which contact zone a particle is going to interact with. The spatial zones are determined by the intersection of geometrical areas defined by the subgroups shown in Fig. 4. Each subgroup is defined geometrically using the projection of auxiliary vectors coming from the geometrical characterization of the tool parametrization.

3.3 Imposition of the contact constraint

When an active set of contacts are determined, the mathematical model of the normal contact constraint is added to the linear momentum balance equation. For each one of the rigid tool surfaces, the outward normal direction **n** is obtained via the next rules: (1) a particle in contact with the flank or rake faces get the normal direction from those planes; (2) the normal direction, for a particle that is in contact with the tool tip contour, is given by the segment that joints the tool center with the particle. When a particle enters in contact with one of the tool surfaces, the normal gap g_N is calculated by the projection of the exceeding distance vector into the corresponding normal direction:

$$g_N = -(\mathbf{x}_I^{n+1} - \bar{\mathbf{x}}_I^{n+1}) \cdot \mathbf{n} \qquad (36)$$

where $\mathbf{x}_I^{n+1}$ is the current position of the particle I and $\bar{\mathbf{x}}_I^{n+1}$ is the corresponding position of the same particle I on the tool surface (Fig. 4).

Fig. 4 Zones of the rigid tool with which a particle can enter in contact
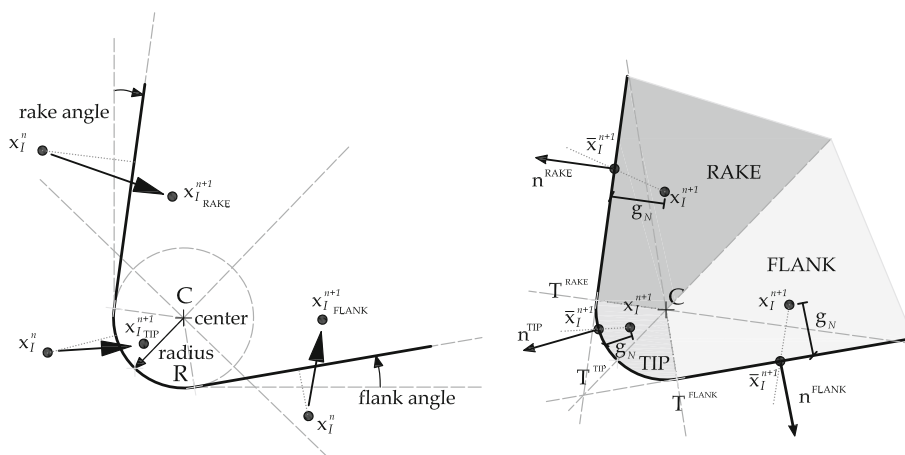
By means of a penalty approach, the constitutive equation for the normal force P_n applied on a particle is

$$\mathbf{P}_N = \begin{cases} \kappa\, \mathbf{g_N} & \text{if } g_N < 0 \\ 0 & \text{otherwise} \end{cases} \tag{37}$$

in the above equation, κ is the penalty coefficient and $\mathbf{g_N} = g_N \mathbf{n}$. It is important to mention that κ must be proportional to the workpiece surface area of the particle entering in contact $\kappa \to \kappa_I$. This is important in order to guarantee that the finite elements satisfy the patch test. The contribution of the contact constraint to the weak form of the linear momentum equation is

$$\int_{\Gamma_{cont}} \eta_i\, \mathbf{P}_N\, n_i\, d\Gamma_{cont} = \mathbf{P}_N \mathbf{n} \tag{38}$$

where $\mathbf{n}$ is the normal vector to the contact surface and η_i are the space weighting functions for the displacement field. For each workpiece boundary particle the gap g_N at the closest point projection is calculated. This is done for each one of the surface zones and then the surface with the minimum gap is the selected one. The resultant contact force applied to the particle is proportional to the gap in the direction to the surface normal. For an implicit integration scheme, the linearization of the contact force is needed to ensure quadratic convergence. The contact force and the contact stiffness matrix for a particle I entering into one of the contact zones are given by:

$$\mathbf{F}_{c\,I} = \kappa_I\, \mathbf{g}_{N\,I}\, \mathbf{n}_I \tag{39}$$

and

$$\mathbf{K}_{cI} = \begin{cases} -\kappa_I\,(\mathbf{n}_I \otimes \mathbf{n}_I) & \rightarrow \text{for rake and flank planes} \\ \kappa_I \left(-\dfrac{R}{\left\| \mathbf{x}_I^{n+1} - \mathbf{x}_C^{n+1} \right\|} \mathbf{n}_I \otimes \mathbf{n}_I + \dfrac{g_N}{\left\| \mathbf{x}_I^{n+1} - \mathbf{x}_C^{n+1} \right\|} \mathbb{1} \right) & \rightarrow \text{for the tip} \end{cases} \tag{40}$$

where the R and $\mathbf{x}_C^{n+1}$ are the radius and the center position defining the tool tip zone, respectively. For κ_I we must ensure it has a value stiffer than the deformable body $\kappa_I \geq E$, being E the elastic modulus of the material. A usual value is

$$\kappa_I \geq 1000\, E \left(\frac{A_I}{A_J^{min}} \right) \tag{41}$$

where A_I is the contributory contact area associated to the node of the deformable body entering in contact with the wall. The area A_J^{min} is the minimum contact surface associated with a contact node.

Figure 5 shows the normal contact forces computed using the explained approach.

4 Validation examples

The examples presented next have been chosen in order to validate the modelling capabilities of the PFEM formulations described in this work. The principal features that we demand are an accurate numerical solution and non-locking numerical effects. In order to assess the numerical behaviour of the PFEM for 3D cases using the mixed $\mathbf{u} - p$ and $\mathbf{u} - \phi$ formulations, we have chosen validation examples involving the large deformation of metal bars. The well-known example of the necking of a bar is presented in Sect. 4.1 and the impact of a bar in Sect. 4.2. The influence in the results of the domain regeneration used by the PFEM is tested in Example 4.2, and in the following cutting examples.

The contact, the elasto-plastic material modeling, and other features of the PFEM presented in the previous sections are tested and validated in the Examples 4.3 and 4.4. Example 4.3 shows a comparison between a 2D and a 3D PFEM simulation of a linear cutting test of a titanium alloy. Example 4.4 applies a physically based model for the 3D modelling of an orthogonal cutting test of an steel work piece.

Fig. 5 Contact forces at particles interacting with rigid walls
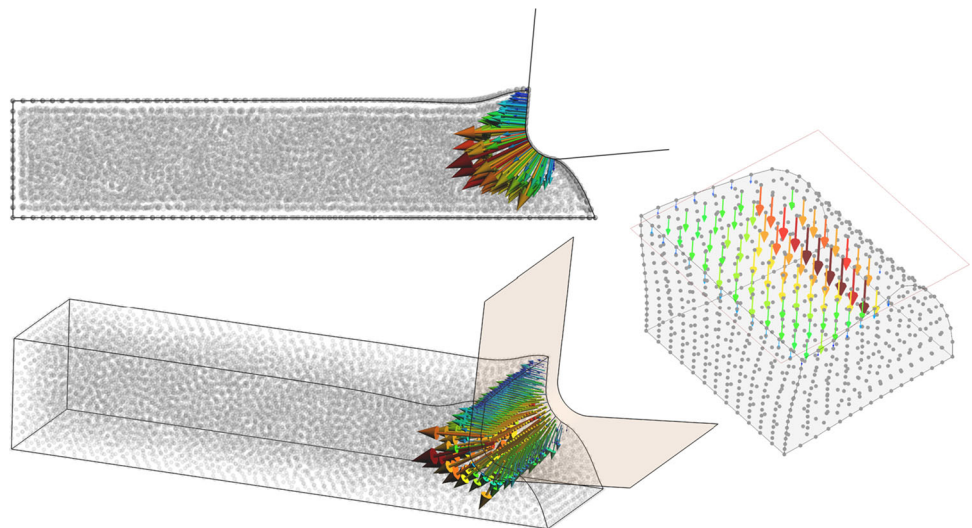
The objective here is to show the capabilities of the PFEM in problems which combine contact, complex geometrical regeneration of the domain and complex constitutive behavior.

The 3D PFEM developments have been implemented in an in-house code, having a limited computational efficiency for the calculations. For this reason we have not run large models, and we will not put much emphasis in the computational cost of the validation examples. This aspect is indeed very important in numerical simulations of practical machining problems and will be analysed in detail in future works. We only can say here that our computations are in the same order of CPU time as using commercial codes.

4.1 Necking of a rectangular bar

In this example a 3D prismatic specimen is loaded by uniform traction forces. The bar has a relation width/thickness/length = 16/4/52 mm (Fig. 6). The bar is assumed to be insulated along its lateral face ($q_n = 0$), while the temperature is held constant and equal to 293.15K on the upper and lower faces. The bar is stretched by applying a constant axial velocity 2 mm/s during 6 seconds. Taking into account the symmetry of the geometry, only one eighth of the specimen is considered for the simulation. The chosen values of thermo-mechanical properties of the specimen correspond to a steel material and are given in Table 1. For this material the *Voce* hardening model presented in Eq. (35) is used.

To solve the problem we use the $\mathbf{u} - p$ and the $\mathbf{u} - \phi$ stabilized element formulations proposed in this work. The simulations are performed under quasi-static conditions with the isothermal implicit split approach proposed by *Simo* [32]. No specific features of the PFEM are used in this exam-
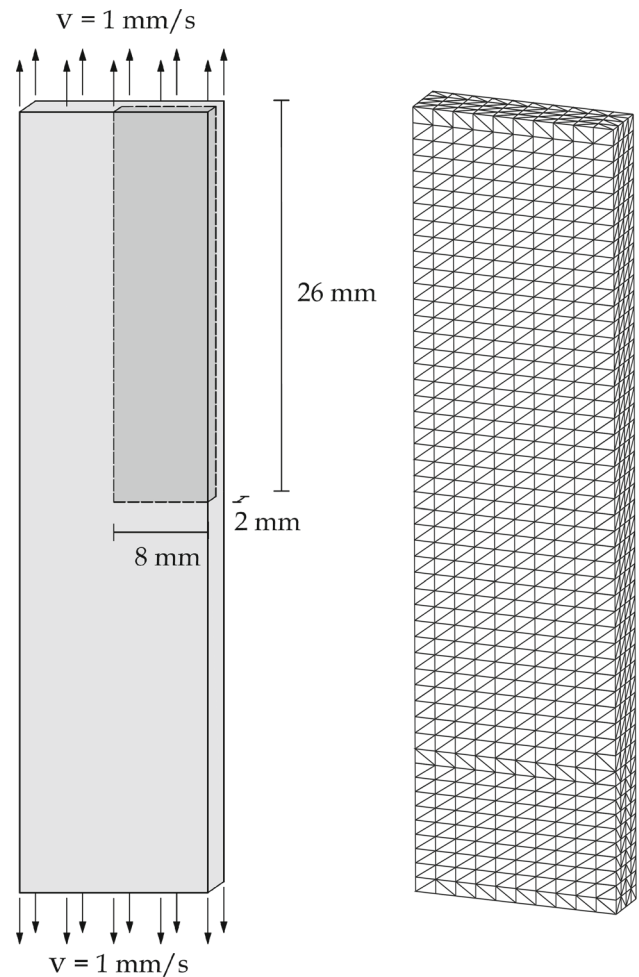

Fig. 6 3D analysis of a nearly adiabatic shear banding traction test benchmark. Problem dimensions for an eighth of the model and initial mesh of 4-noded tetrahedra with 10 × 4 × 50 divisions

Table 1 Steel properties for the *Voce* model

Young modulus	E	$206.9 \cdot 10^3$	MPa
Dissipation factor	χ	0.9	
Thermal capacity	c	$0.46 \cdot 10^9$	$mm^2/s^2 K$
Density	ρ	$7.8 \cdot 10^{-9}$	Ns^2/mm^4
Expansion coefficient	α	$1 \cdot 10^{-5}$	K^{-1}
Yield stress	σ_y	450	MPa
Flow stress softening	w_0	0.002	K^{-1}
Reference temperature	θ_0	293.15	K
Linear hardening	H	129.24	MPa
Hardening softening	w_h	0.002	K^{-1}
Saturation hardening	K_{inf}	715	MPa
Hardening exponent	δ	16.93	

ple. The purpose is to evaluate the thermo-hyperelastoplastic model and the stabilized formulations for 3D tetrahedra.

Figures 7 and 8 show the pressure, temperature, *Von-Mises* stress and plastic strain fields for the mixed $\mathbf{u} - p$ and $\mathbf{u} - \phi$ stabilized element formulations. The results are very similar in both cases, the formulations do not block in the softening branch and predict the thermo-elastoplastic behaviour correctly. In Fig. 9 the vertical reaction loads are depicted. Similar forces are predicted during the strain-hardening part of the force displacement curve. However, in the strain-softening branch the predicted forces are different. These differences also happen when comparing other formulations [23,32,40,41] (Fig. 10).

The geometry and conditions of this 3D example have been studied in [32]. In this reference the modelling is done using hexahedra elements. The results shown are the deformed geometry (with a concave curvature in the direction of the width and a convex curvature in the direction of the thickness), the increment of temperature of 85.04K and the maximum principal stress of 117.7MPa at t=6s. In our results, the deformation obtained is the same. However we
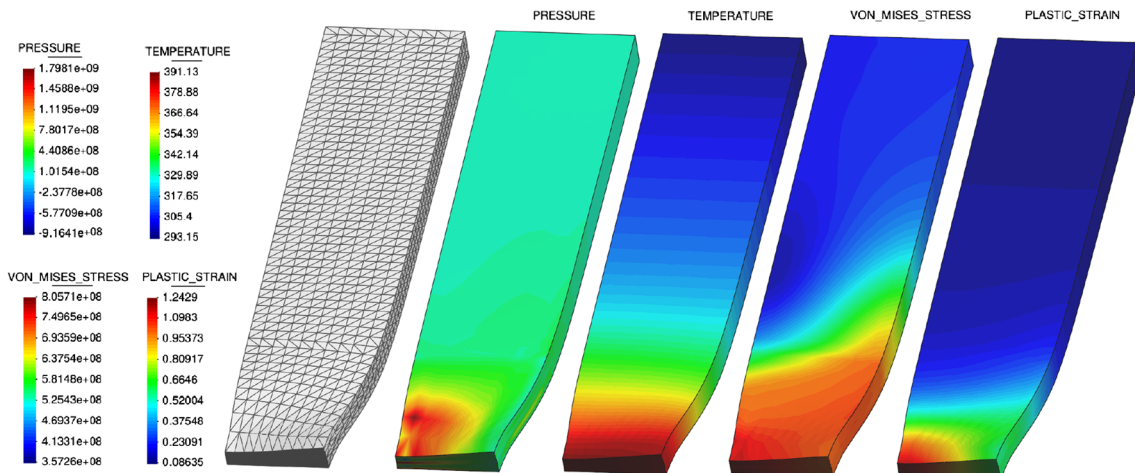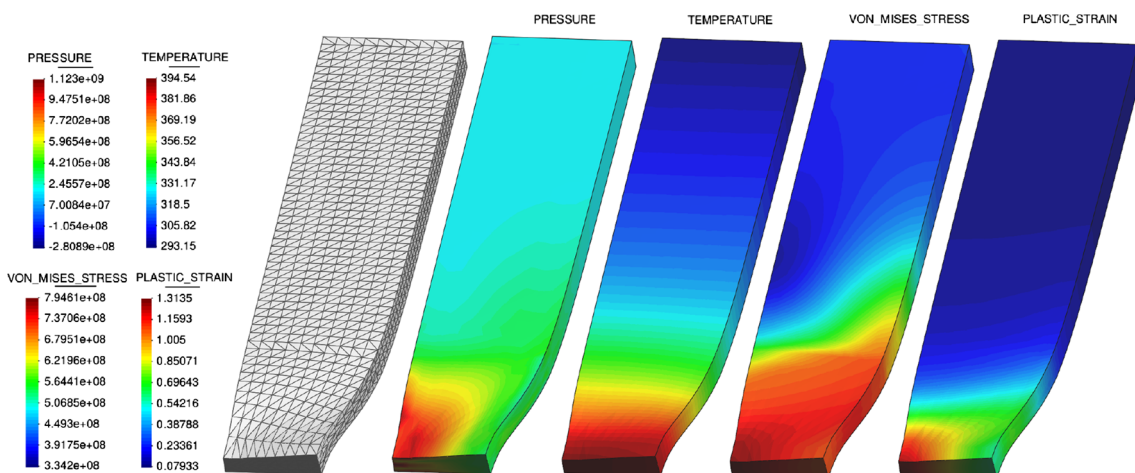

Fig. 7 Three-dimensional analysis of a nearly adiabatic shear banding traction test benchmark. Problem results for the $\mathbf{u} - p$ formulation

Fig. 8 Three-dimensional analysis of a nearly adiabatic shear banding traction test benchmark. Problem results for $\mathbf{u} - \phi$ formulation

Fig. 9 3D nearly adiabatic shear banding. Load/Displacement curve for the $\mathbf{u} - p$ and $\mathbf{u} - \phi$ formulations. Bar with dimensions = 16/4/52 mm
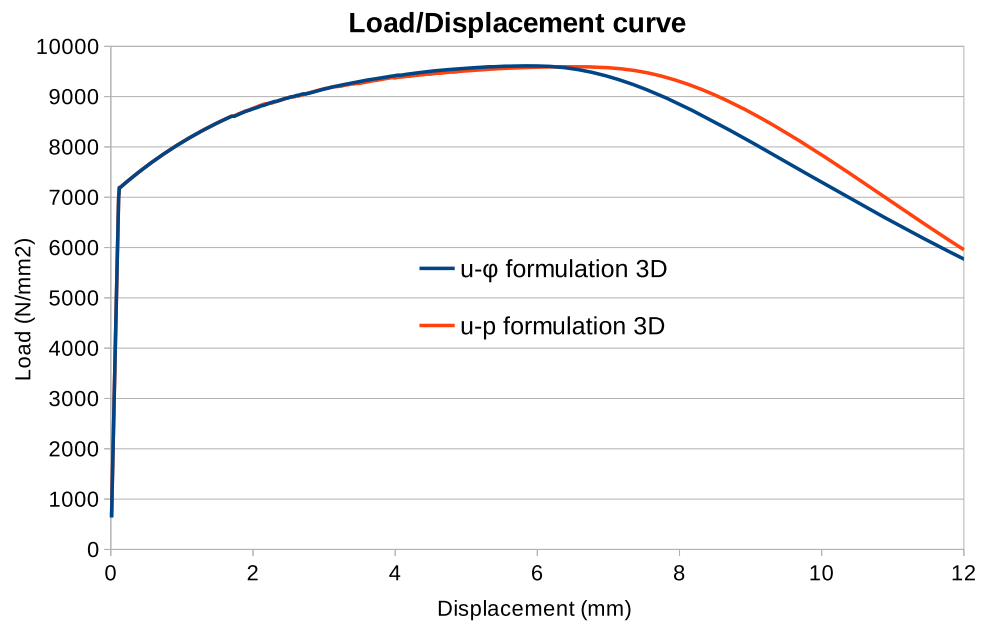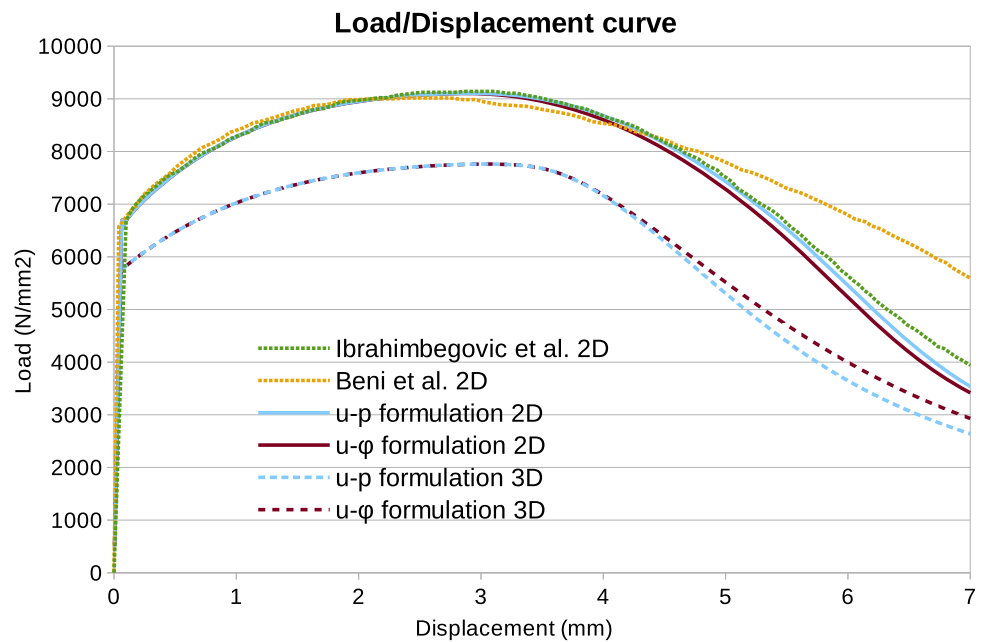
Load/Displacement curve

(Load (N/mm2) vs Displacement (mm))

— u-φ formulation 3D
— u-p formulation 3D

Fig. 10 2D Plane strain and 3D nearly adiabatic shear banding. Load/Displacement curve for the several formulations and authors [40,41]. Bar with dimensions = 12.826/1/53.334 mm

Load/Displacement curve

(Load (N/mm2) vs Displacement (mm))

········ Ibrahimbegovic et al. 2D
········ Beni et al. 2D
— u-p formulation 2D
— u-φ formulation 2D
- - - u-p formulation 3D
- - - u-φ formulation 3D

get sligthly larger values, with a temperature increment of $97.98K$ and $101.39K$ and a maximum principal stress of 125.9MPa and 133.0MPa for the $\mathbf{u} - p$ and the $\mathbf{u} - \phi$ formulations, respectively. Most of the examples found in the literature simulate the necking of a rectangular bar with a width/thickness/length ratio= 12.826/1/53.334 mm using 2D plain strain models [23,40,41]. Looking for a more comprehensive comparison we have also simulated these cases using 2D plain strain and 3D models. Figure 10 shows the results obtained compared with results from the literature. It is shown that the 2D plain strain models give a similar response. We note that the plain strain models do not capture

the reduction of the bar thickness giving an over-prediction of the forces compared with 3D models. Considering this fact we can conclude that both 3D formulations developed in this work predict the force in the softening branch in a similar way and in agreement with other published results.

4.2 Taylor impact test for a cylindrical bar

The test consists of the impact of a cylindrical bar with an initial velocity of $227\,m/s$ against a rigid wall. The bar has an initial length of $32.4mm$ and an initial radius of $3.2\,mm$ (Fig. 11). Material properties of the bar are typical of copper: den-
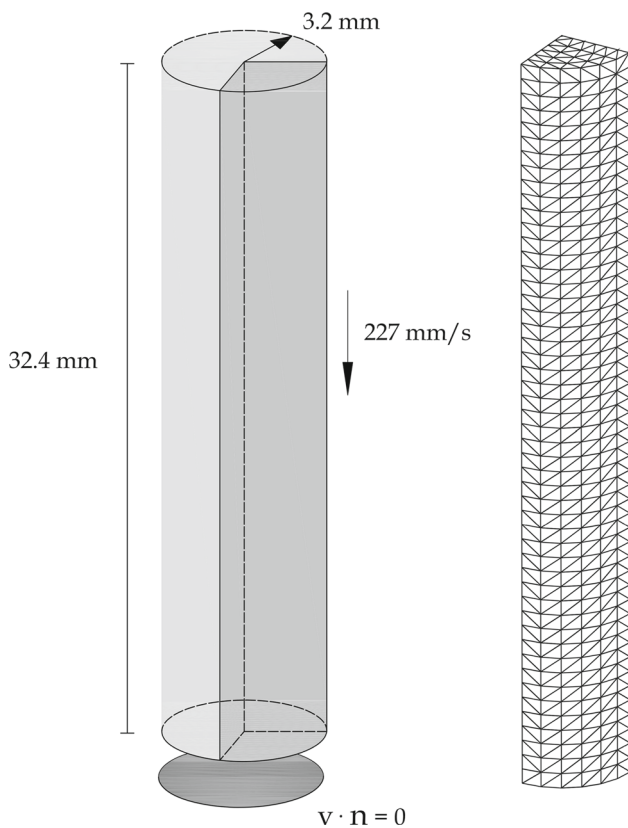
Fig. 11 Taylor impact test. Problem dimensions and the initial structured mesh of 6 × 50 divisions

sity $\rho = 8930 \, kg/m^3$, Young's modulus $E = 1.17 \cdot 10^5 \, MPa$, Poisson's ratio $\nu = 0.35$, initial yield stress $\sigma_y = 400 \, MPa$ and hardening modulus $H = 100 \, MPa$. An interval of $80 \, \mu s$ has been analyzed, which corresponds to the neutralization of the impact.

Starting with the same initial mesh, the problem has been solved with the $\mathbf{u} - p$ and the $\mathbf{u} - \phi$ stabilized formulations proposed in this work. Looking at the analysis results some parts of the mesh gets very deformed and the elements that received first the impact experience large plastic deformations. This yields results somehow conditioned by the mesh shape. In order to improve this aspect, in these examples the mesh has been continuously updated during the analysis using the PFEM with the procedure explained in Sect. 2.5. However, in this example, there are boundary particles belonging to symmetric constrained walls that have to be preserved. Therefore, the boundary particles and boundary faces connectivities have not been modified during the analysis. The domain regeneration has been applied by reconnecting the inside domain, removing inside particles if the distance between them is too close, and inserting new particles if the plastic dissipation reaches a threshold value.

The results for the displacements, the plastic strain, the pressure and the *Von-Mises* stress are depicted in Figs. 12 and 13 for the $\mathbf{u} - \phi$ and $\mathbf{u} - p$ the cases, respectively. The pressure and the stress distributions are a little bit nicer for
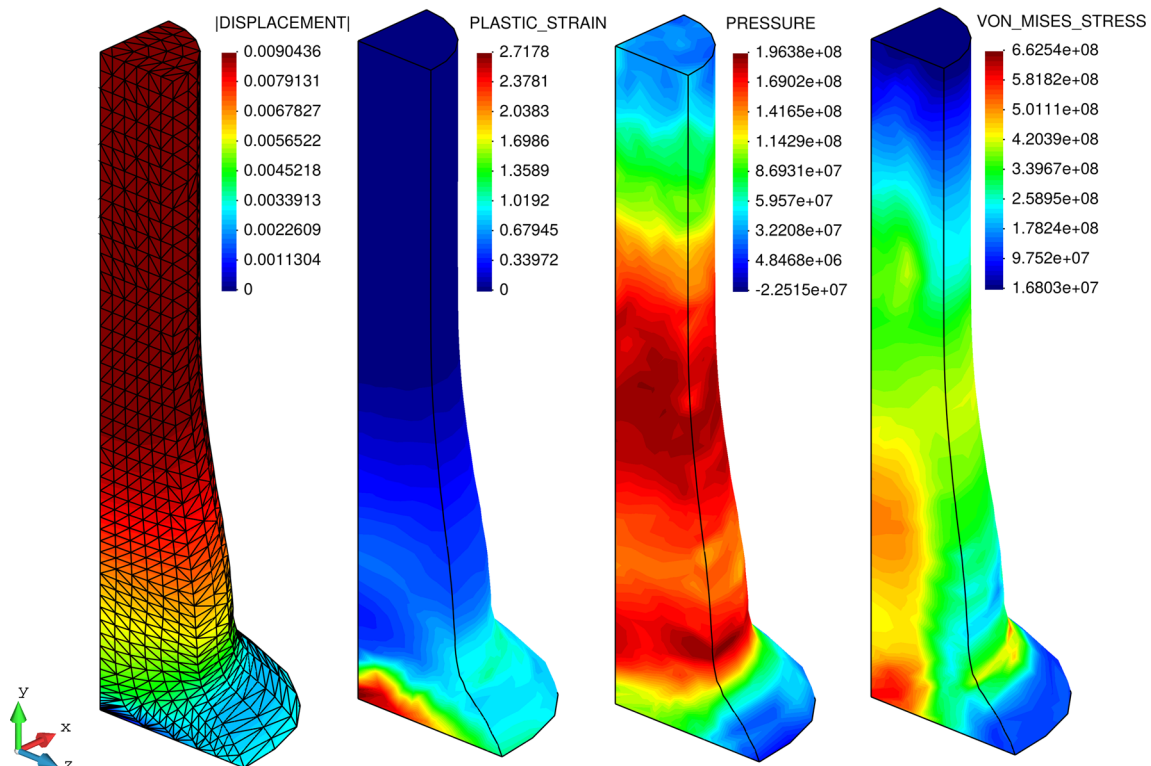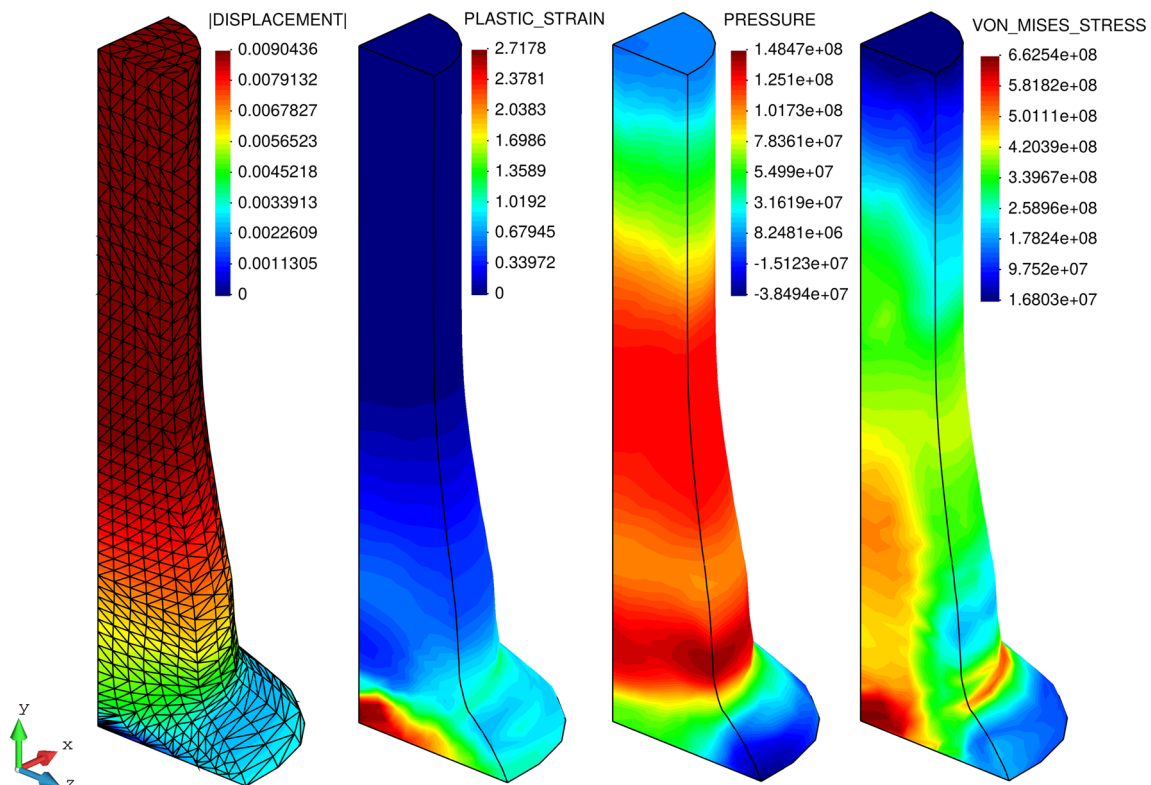

Fig. 12 Final mesh displacement, equivalent plastic strain distribution, Pressure field, and *Von-Mises* Stress at $80\mu s$ after the impact for the PFEM $\mathbf{u}$-ϕ formulation with continuous remeshing

Fig. 13 Final mesh displacement, equivalent plastic strain distribution, Pressure field, and *Von-Mises* Stress at $80\mu s$ after the impact for the PFEM **u**-p formulation with continuous remeshing

the $\mathbf{u} - p$ formulation. The computed plastic strain, however, is almost the same in both cases. Looking at the results of Figs. 12 and 13, the values obtained and the deformed configuration are very similar for both formulations.

The final geometry of the bar in any of the formulations is in good agreement with the published results [23,37–39]. No locking is not present in the solution. The final radius in the base of the bar obtained using the $\mathbf{u} - p$ formulation is $6.47\,mm$ and using the $\mathbf{u} - p$ formulation is $6.43\,mm$. The results presented in the literature [23,37–39], calculated with 2D axisymmetric models and 3D models, vary from a $6.99\,mm$ to $7.24\,mm$ depending on the method and the stabilization technique used. The values for the equivalent plastic strain and pressure fields obtained with the PFEM coincide well with those given by FIC stabilization technique and by the CBS formulation [37].

4.3 Linear cutting test of titanium alloy.

In order to validate the PFEM strategy with a 3D machining test case, we have studied the cutting of a rectangular block of Ti6Al4V alloy of at $200\,m/min$, with a tool radius of $0.4\,mm$, a rake angle of $0°$ and a cutting depth of $0.6\,mm$. The workpiece has a length of $3.7\,mm$, a width of $1.8\,mm$ and a thickness of $1\,mm$. The model is depicted in Fig. 14.
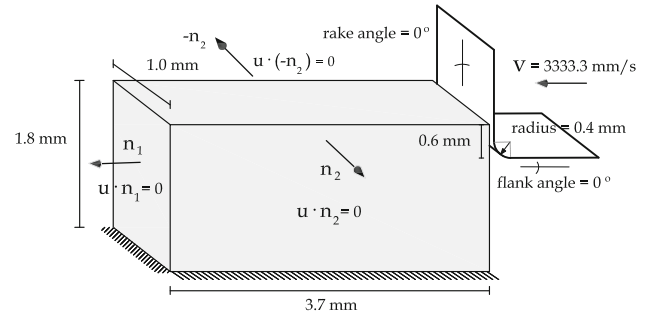

Fig. 14 3D Linear cutting test model

The material used for the work piece is the one evaluated by a high strain rate compression in [36]. A summary of all the input parameters is given in Table 2. The tool has been assumed to be mechanically rigid and the friction and the thermal exchange between the work piece and the tool are neglected. The problem has been modelled using a 2D and a 3D approach. The applied boundary conditions are shown in Fig. 14. The normal displacement for the lateral and end walls of the work piece has been constrained. The base of the work piece is clamped (Fig. 14).

The solution scheme used in the present example is based on the isothermal implicit scheme [23] with the mixed $\mathbf{u} - p$ formulation described in this paper. The domain regeneration

Table 2 Ti6Al4V alloy properties for the rate dependend *Johnson-Cook* model

Young modulus	–	E	$210.3 \cdot 10^3$	MPa
Poisson ratio	–	ν	0.3	
Density	–	ρ	$7.9 \cdot 10^{-9}$	Ns^2/mm^4
Johnson's Cook A constant	–	A	782.7	MPa
Johnson's Cook B constant	–	B	498.4	MPa
Johnson's Cook C constant	–	C	0.028	
Johnson's Cook n constant	–	n	0.28	
Johnson's Cook m constant	–	m	1	
Expansion coefficient	α	$1 \cdot 10^{-5}$	K^{-1}	
Thermal capacity	–	c	$0.445 \cdot 10^9$	$mm^2/s^2 K$
Thermal conductivity	–	k	14	N/sK
Fusion temperature	–	θ_f	1873.15	K
Reference strain rate	–	$\dot{\varepsilon}_0$	$1 \cdot 10^{-4}$	s^{-1}
Reference temperature	–	θ_0	293.15	K

is based on the PFEM technique presented in Sect. 2.5. Insertion and removal of particles is used here to save computing time and in order to improve the localization phenomenon. Material separation in front of the tool has been modeled by considering the chip formation process as a pure deformation where material flows visco-plastically around the tool tip.

Figure 15 shows the results for the strain rate contours in several time instants. A comparison of the results for the 2D and 3D simulations is done. The value of strain-rate is depicted on the particles in the central section of the 3D case. The 2D and the 3D solutions are not exactly the same, although in both cases strains are concentrated near the shear plane and along the rake face, as expected. We remark that the boundary conditions applied in the 3D case tried to be as close as possible to the conditions in the 2D solution. However, a perfect matching is not possible and there are some remarkable differences in the deformed configuration. When the tool has travelled 2.2*mm* the 3D model has 23814 4-noded tetrahedra and 4622 particles (i.e. nodes). For the 2D case the model has 3163 3-noded triangles and 1696 particles (i.e. nodes). We note that the number of particles of a section corresponding to a 3D cut (1877 nodes) is similar in the 2D case (1696 nodes), but the distribution of the particles marks the difference in the accuracy of the results.

The temperature field for the workpiece in the 2D and 3D cases is also depicted in Fig. 16. The maximum temperature is 1539.5 *K* and takes place along the rake face and tool tip. Figure 17 shows the cutting forces applied on the tool obtained in the 2D and 3D analyses. In the 3D case the forces are a little big larger because the boundary restrains has a big influence on the results, as some material deforms and accumulates behind the chip. The cutting forces reach a steady state as expected for a continuous chip formation.

4.4 3D orthogonal cutting test of steel

In this example we simulate a 3D orthogonal cutting test of a AISI 316L steel. A physically based plasticity model is used to reproduce the behaviour of the workpiece. The model, referenced in Sect. 2.4, is based on the dislocation density and vacancy concentration. The details and the material properties feeding the constitutive law can be found in [24,35]. The general material parameters for the AISI 316L steel are summarized in Table 3.

The problem geometry and kinematics are depicted in Fig. 14, but the lateral walls of the workpiece have no imposed displacements. These conditions do not intend to reproduce a 2D cut like in the previous example, quite the opposite.

The deformation results for the 3D cut are shown in Fig. 18. It can be observed that the chip is being formed in the front of the tool due to plastic deformations. However, because the movements in the lateral walls are not restrained, the material also flows towards these directions.

The deformed configuration when the tool has moved 1.98 *mm* is shown in Fig. 19. In the same figure the temperatures and the *Von-Mises* stress fields at this instant are given. The plastic strain rate is depicted using a central cut of the workpiece. The velocity of the plastic strain travels from the tool tip to the surface of the chip formation, as expected. At this moment the primary and secondary shear zones have collapsed to a largest zone in front of the tool.

The distribution of damage, in terms of dislocations suffered by the material, is depicted in Fig. 20. The temperature level and the increase on the dislocation density controls the hardening of the material.

The 3D modelling, together with the use of the material physical model, allow a more detailed microscopic study of the cutting zone. This contributes to a good understanding of

Fig. 15 Strain rates are depicted on particles at the deformed configuration of the workpiece. Results shown for several positions of the tool path showing a central cut of the 3D model and section of the 2D case (**u** is the tool displacement)
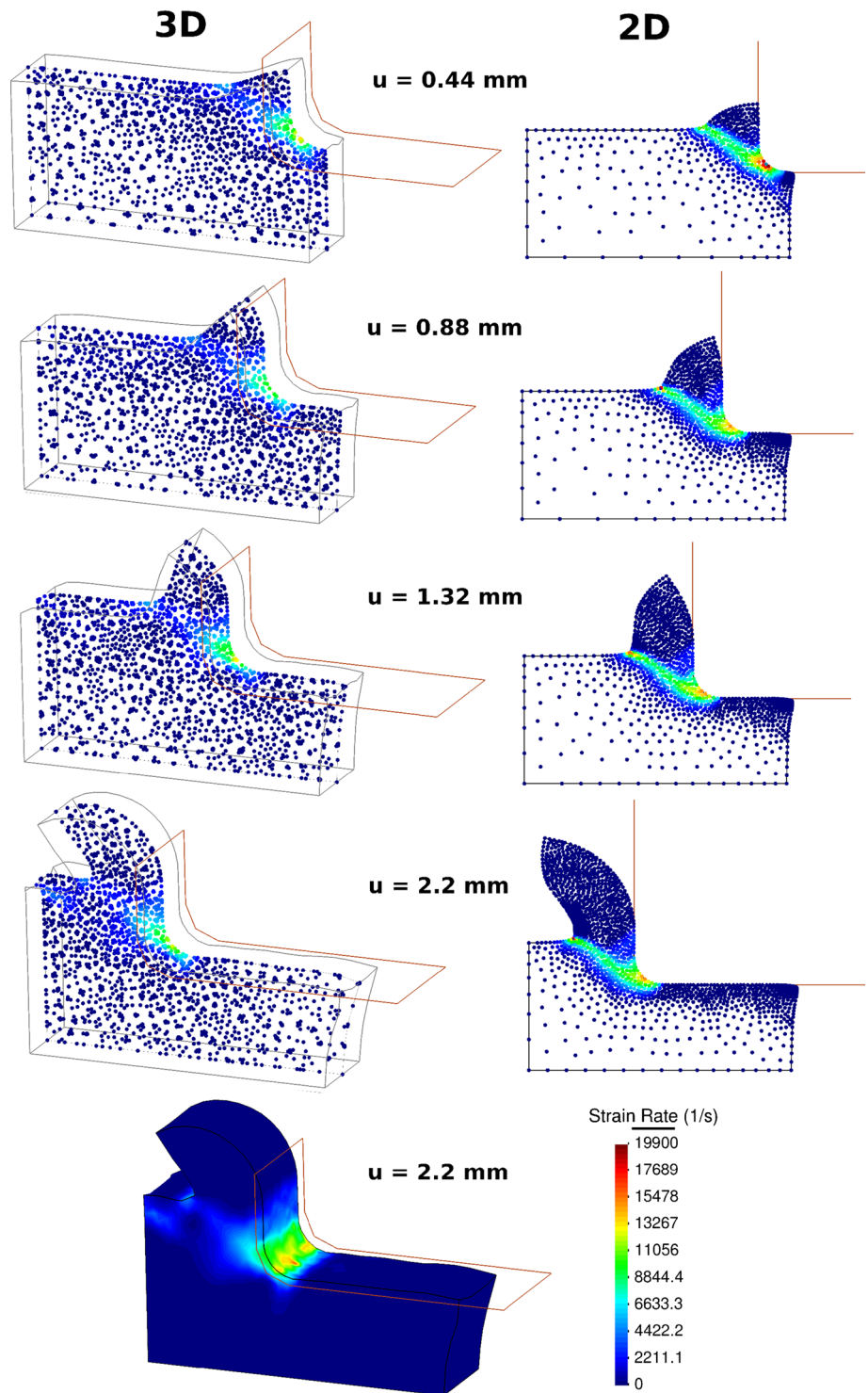
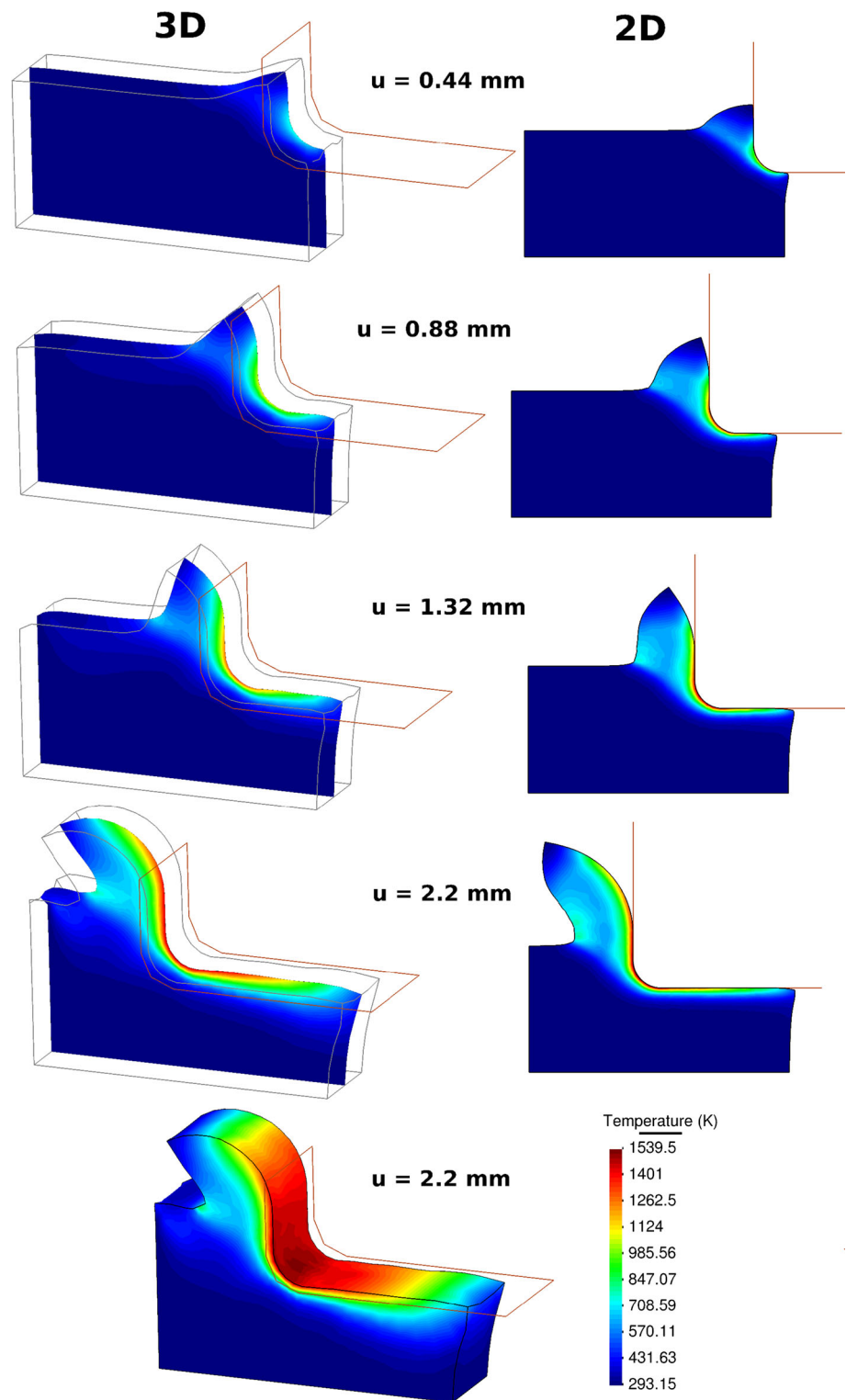**Fig. 16** Temperatures are depicted in the deformed configuration of the workpiece. Results shown for several positions of the tool path showing a central cut of the 3D model and section of the 2D case (**u** is the tool displacement)

Fig. 17 Cutting Force versus tool displacement
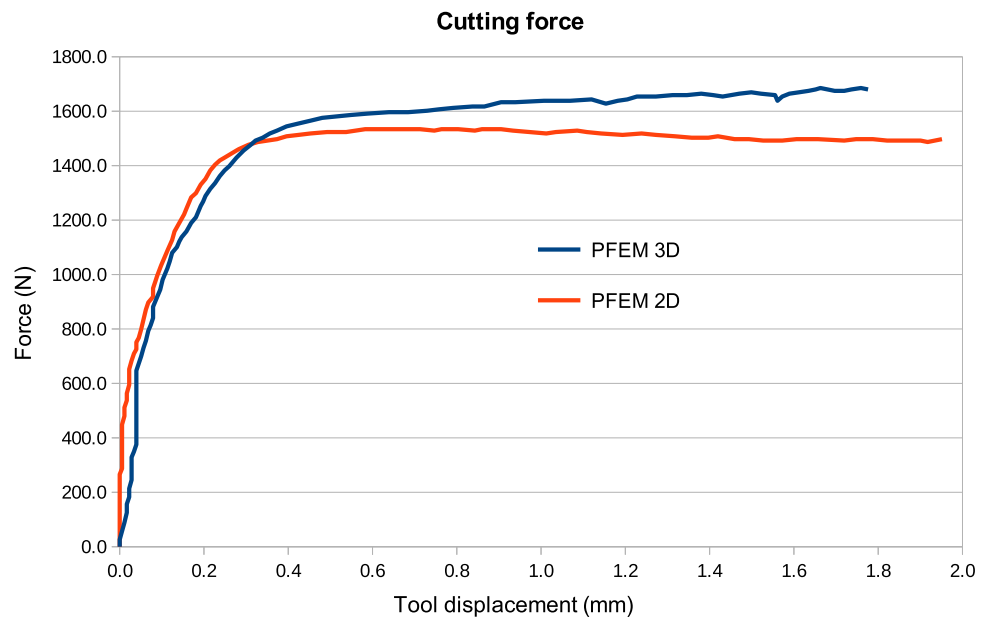
Table 3 AISI 316L steel properties

Young modulus	–	E		$210 \cdot 10^3$	MPa
Poisson ratio	–	ν		0.3	
Density	–	ρ		$7.9 \cdot 10^{-9}$	Ns^2/mm^4
Expansion coefficient	α		$1.55 \cdot 10^{-5}$	K^{-1}	
Thermal capacity	–	c		$0.445 \cdot 10^9$	$mm^2/s^2 K$
Thermal conductivity	–	k		14	$N/s K$

Fig. 18 Deformed configuration of the workpiece for several instance of cutting tool path
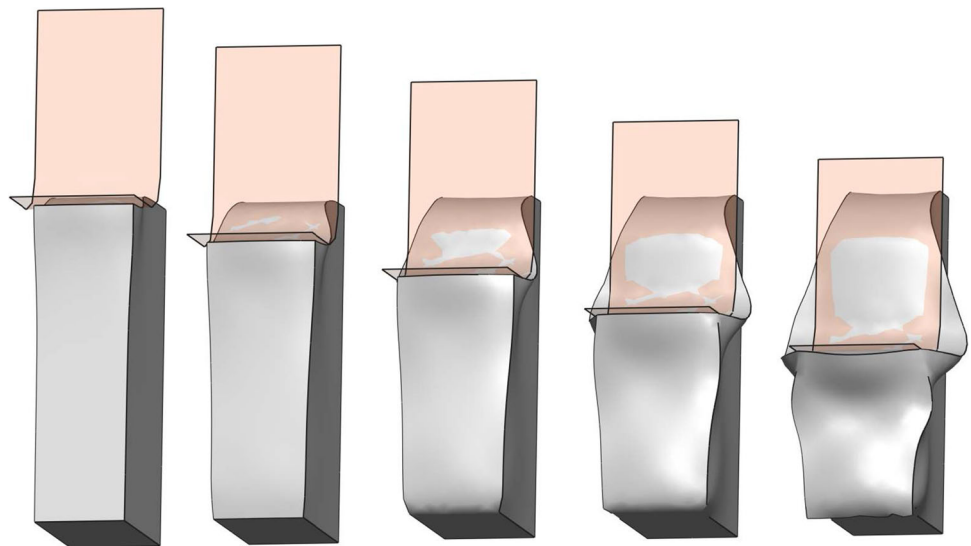
Fig. 19 Results at the last deformed configuration of the analysis when the tool has moved 1.98 mm
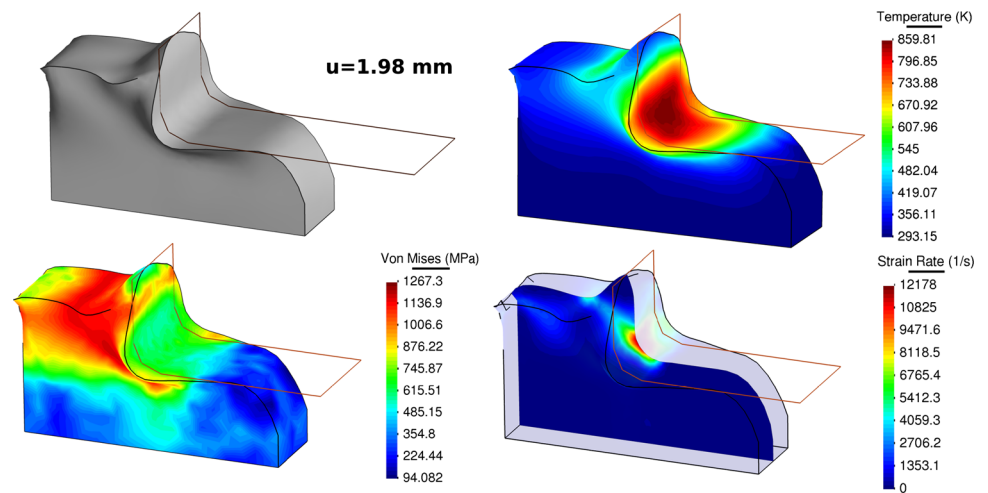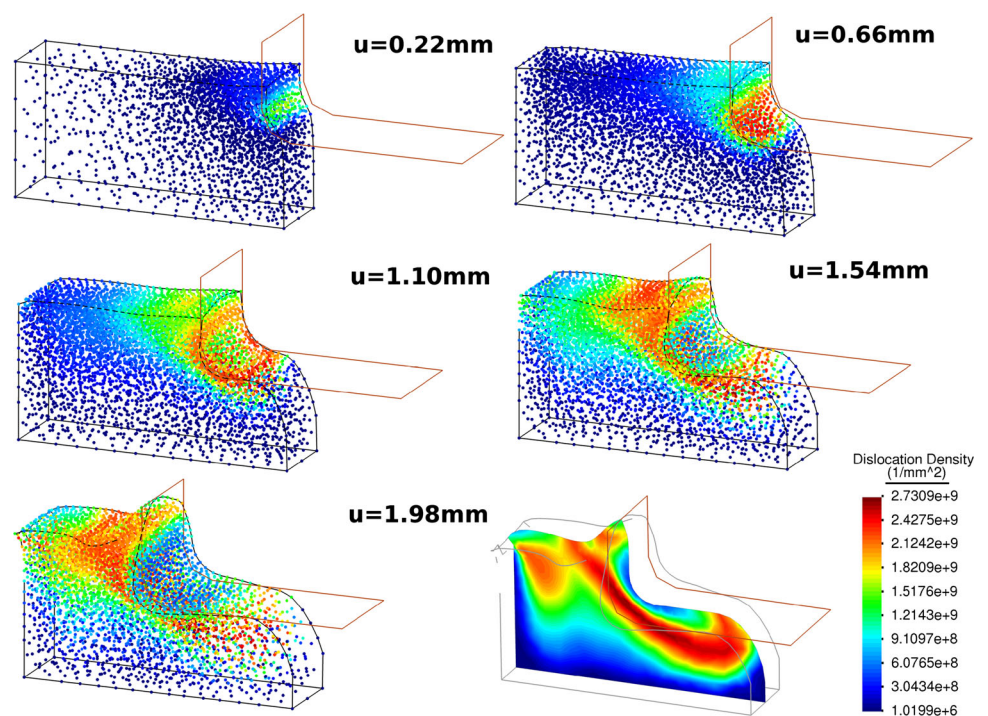

Fig. 20 Dislocation densities depicted on particles at the deformed configuration of the workpiece. Results shown for several positions of the tool path. Showing a central cut of the 3D model at the last position

the interaction between strain hardening, thermal softening and shear localization during the chip formation.

5 Conclusions

In this work we have upgraded the Particle Finite Element Method (PFEM) in order to face the simulation of 3D cutting problems exhibiting large deformations, thermal coupling and tool-workpiece mechanical contact conditions. The presented extension of the PFEM includes the use of the mixed $\mathbf{u} - p$ and $\mathbf{u} - \phi$ formulations for large strains. These formulations are extended to the solution of coupled thermo-mechanical problems using 3-simplex ele-

ments and elasto-plastic constitutive models. The PFEM has been readapted to face 3D continuous domain regeneration with an enhanced strategy for insertion of particles and a *constrained Delaunay* tetrahedralization. New procedures to improve the accuracy of the surface definition and the elements shape via smooth re-collocation of particles have been integrated in the generation of the calculation domain.

For the modeling of cutting problems rigid contact constraints have been used. The development of rigid tool tip sub-systems for an easy contact detection and a smooth application of the contact forces in the balance equations have been presented. More advanced techniques can be applied to introduce deformable and frictional contact conditions,

considering thermal transfer, which will improve the results. This improvement is an objective of the future work.

The combination of the techniques mentioned above leads to a PFEM able to handle the modelling of 3D metal cutting processes. The modelling capacity of the mixed $\mathbf{u} - p$ and $\mathbf{u} - \phi$ formulations has been tested with two classical large deformation problems in thermo-plasticity. The results obtained agree with other simulation techniques.

The capabilities the PFEM for modelling 3D cutting problems, have been demonstrated with the analysis of two representative numerical simulations of 3D orthogonal cutting tests. A comparison with the 2D modelling of the cut has been made in one of the examples, providing very similar results to the 3D solution. It is interesting that the 2D solution yielded good predictions of the cutting forces, while it simplifies substantially the actual 3D boundary constraints.

The numerical solutions obtained with the PFEM provide accurate results for the chip thickness, the contact length, the cutting and feed forces, the distribution of the strain rate, strains, temperatures, and *von Mises* stress, among other process variables that are very costly and difficult to measure experimentally. The versatility of the 3D PFEM approach developed in this work has many advantages for the simulation of practical cutting problems.

Compliance with ethical standards

Declarations Not applicable.

References

1. Belytschko T, Liu WK, Moran B (2000) Nonlinear finite element for continua and structures. Wiley, England
2. Bonet J, Wood RD (1997) Nonlinear continuum mechanics for finite element analysis. Cambridge University Press, United Kingdom
3. Chiumenti M, Valverde Q, Agelet de Saracibar C, Cervera M (2004) A stabilized formulation for incompressible plasticity using linear triangles and tetrahedra. Int J Plast 20:1487–1504
4. Bochev PB, Dohrmann CR, Gunzburger MD (2008) Stabilization of low-order mixed finite elements for the stokes equations. SIAM J Numer Anal 44:82–101
5. Calvo N, Idelsohn S, Onate E (2003) The extended Delaunay tellesation. Engineering Computations: Int J for Computer-Aided Engineering 20:583–600
6. Carbonell JM (2009) Modeling of ground excavation with the particle finite element method. PhD thesis, Universitat Politècnica de Catalunya (UPC), Barcelona
7. Carbonell JM, Oñate E, Suárez B (2009) Modeling of ground excavation with the particle finite-element method. J Eng Mech 136:455–463
8. Carbonell JM, Oñate E, Suárez B (2013) Modelling of tunnelling processes and rock cutting tool wear with the particle finite element method. Comput Mech 52:607–629
9. Delaunay BN (1934) Sur la Sphère Vide, A la memoire de Georges Voronoi. Otdelenie Matematicheskii i Estestvennyka Nauk 7:793–800
10. Dohrmann CR, Bochev PB (2004) A stabilized finite element method for the Stokes problem based on polynomial pressure projections. Int J Numer Methods Fluids 46:183–201
11. Idelsohn SR, Oñate E, Del Pin F (2004) The particle finite element method: a powerful tool to solve incompresible flows with free-surfaces and breaking waves. Int J Numer Methods Eng 61:964–989
12. Joe B, Wang CA (1993) Duality of constrained voronoi diagrams and delaunay triangulations. Algorithmica 9 4:142–155
13. Johnson GR, Cook WH (1983) A constitutive model and data for metals subjected to large strains, high strain rates and high temperatures. In: Proceedings of 7th international symposium on ballistics, Hague, Netherlands, pp 1–7
14. Oliver J, Cante JC, Weyler R, González C, Hernández J (2007) Particle finite element methods in solid mechanics problems. Comput Methods Appl Sci 7:87–103
15. Oñate E, Idelsohn SR, Del Pin F, Aubry F (2004) The particle finite element method: an overview. Int J Numer Methods Eng 1(2):964–989
16. Oñate E, Celigueta MA, Idelsohn SR (2006) Modeling bed erosion in free surface flows by the particle finite element method. Acta Geotech 1:237–252
17. Oñate E, Idelsohn SR, Celigueta MA, Rossi R (2008) Advances in the particle finite element method for the analysis of fluid multibody interaction and bed erosion in free surface flows. Comput Methods Appl Mech Eng 197:1777–1800
18. Oñate E, Franci A, Carbonell JM (2013) Lagrangian formulation for finite element analysis of quasi-incompressible fluids with reduced mass losses. Int J Numer Methods Fluids 74:699–731
19. Oñate E, Franci A, Carbonell JM (2014) A particle finite element method for analysis of industrial forming processes. Comput Mech 54:85–107
20. Marusich TD, Ortiz M (1995) Modelling and simulation of high-speed machining. Int J Numer Methods Eng 38:3675–3694
21. Rodríguez JM (2014) Numerical modeling of metal cutting processes using the particle finite element method(PFEM). PhD thesis, Universitat Politècnica de Catalunya (UPC), Barcelona
22. Rodríguez JM, Cante JC, Oliver J (2015) On the numerical modelling of machining processes via the particle finite Element method (PFEM). CIMNE: Barcelona 156:186
23. Rodríguez JM, Carbonell JM, Cante JC, Oliver J (2016) The particle finite element method (PFEM) in thermo-mechanical problems. Int J Numer Methods Eng. https://doi.org/10.1002/nme.5186
24. Rodríguez JM, Jonsén P, Svoboda A (2017) Simulation of metal cutting using the particle finite-element method and a physically based plasticity model. Comput Particle Mech 4:35–51 Wiley
25. Rodríguez JM, Jonsén P, Svoboda A (2016) A particle finite element method for machining simulations. In: Papadrakakis M, Papadopoulos V, Stefanou G, Plevris V (eds) ECCOMAS congress: 2016 VII European congress on computational methods in applied sciences and engineering, Crete island, Greece, vol 1. National Technical University of Athens, Athens, pp 539–553
26. Rodríguez JM, Carbonell JM, Cante JC, Oliver J (2017) Continuous chip formation in metal cutting processes using the particle finite element method (PFEM). Int J Solids Struct 120:81–102

27. Rodríguez JM, Carbonell JM, Cante JC, Oliver J, Jonsén P (2017) Generation of segmental chips in metal cutting modeled with the PFEM. Comput Mech 1:1–17

28. Rodríguez JM, Carbonell JM, Jonsén P (2020) Numerical methods for the modelling of chip formation. Arch Comput Methods Eng SP - 387 27:387–412

29. Shewchuk JR (1998) A condition guaranteeing the existence of higher-dimensional constrained Delaunay triangulations. Proceedings of the fourteenth annual symposium on computational geometry. ACM, Minneapolis, MN, USA, pp 76–85

30. Simo JC (1988) A framework for finite strain elastoplasticity based on maximum plastic dissipation and the multiplicative decomposition: part I. continuum formulation. Comput Methods Appl Mech Eng 666:199–219

31. Simo JC (1988) A framework for finite strain elastoplasticity based on maximum plastic dissipation and the multiplicative decomposition: Part II. Computational aspects. Comput Methods Appl Mech Eng 68:1–31

32. Simo JC, Miehe C (1992) Associative coupled thermoplasticity at finite strains: formulation, numerical analysis and implementation. Comput Methods Appl Mech Eng 98:41–104

33. Simo JC, Hughes TJR (1998) Computational inelasticity. Springer, New York

34. Voce E (1955) A practical strain hardening function. UK Metall Br J Metals 51:219–226

35. Svoboda A, Wedberg D, Lindgren L-E (2010) Simulation of metal cutting using a physically based plasticity model. Model Simul Mater Sci Eng 18(7):075005 pp. 1-19

36. Lee W-S, Lin C-F (1998) High-temperature deformation behaviour of Ti6Al4V alloy evaluated by high strain-rate compression tests. J Mater Process Technol 75(1):127–136

37. Rojek J, Oñate E, Taylor RL (2006) CBS-based stabilization in explicit solid dynamics. Int J Numer Methods Eng 66:1547–1568

38. Bonet J, Burton AJ (1998) A simple average nodal pressure tetrahedral element for incompressible and nearly incompressible dynamic explicit applications. Commun Numer Methods Eng 14:437–449

39. De Micheli PO, Mocellin K (2009) A new efficient explicit formulation for linear tetrahedral elements non-sensitive to volumetric locking for infinitesimal elasticity and inelasticity. Int J Numer Methods Eng 79:45–68

40. Ibrahimbegovic A, Chorfi L (2002) Covariant principal axis formulation of associated coupled thermoplasticity at finite strains and its numerical implementation. Int J Solids Struct 39:499–528

41. Tadi Beni Y, Movahhedy MR (2010) Consistent arbitrary Lagrangian Eulerian formulation for large deformation thermomechanical analysis. Int J Solids Struct Mater Des 31:3690–3702

42. Edelsbrunner H, Mucke EP (1994) Three dimensional alpha shapes. ACM Trans Graph 13:43–72

43. Zienkiewicz OC, Zhu JZ (1992) The superconvergent patch recovery and a posteriori error estimates. Part 1: The recovery technique. Int J Numer Methods Eng 33:1331–1364

44. Zienkiewicz OC, Zhu JZ (1992) The superconvergent patch recovery and a posteriori error estimates. Part 2: error estimates and adaptivity. Int J Numer Methods Eng 33:1365–1382